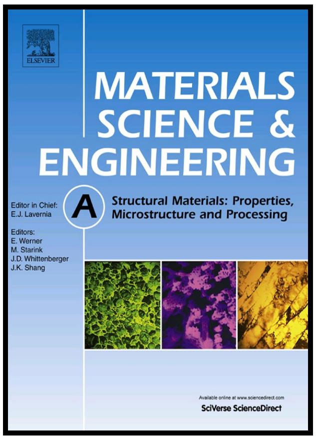
www.elsevier.com/locate/msea

Effect of Aging Temperature on Phase Decomposition and Mechanical Properties in Cast Duplex Stainless Steels

Sarah Mburu, R. Prakash Kolli, Daniel E. Perea, Samuel C. Schwarm, Arielle Eaton, Jia Liu, Shiv Patel, Jonah Bartrand, Sreeramamurthy Ankem

PII: S0921-5093(17)30299-X
DOI: http://dx.doi.org/10.1016/j.msea.2017.03.011
Reference: MSA34794

To appear in: *Materials Science & Engineering A*

Received date: 8 December 2016
Revised date: 2 March 2017
Accepted date: 3 March 2017

Cite this article as: Sarah Mburu, R. Prakash Kolli, Daniel E. Perea, Samuel C Schwarm, Arielle Eaton, Jia Liu, Shiv Patel, Jonah Bartrand and Sreeramamurth Ankem, Effect of Aging Temperature on Phase Decomposition and Mechanica Properties in Cast Duplex Stainless Steels, *Materials Science & Engineering A* http://dx.doi.org/10.1016/j.msea.2017.03.011

Effect of Aging Temperature on Phase Decomposition and Mechanical Properties in Cast Duplex Stainless Steels

Sarah Mburu[1,*], R. Prakash Kolli[1], Daniel E. Perea[2], Samuel C. Schwarm[1], Arielle Eaton[2], Jia Liu[2], Shiv Patel[1], Jonah Bartrand[2], and Sreeramamurthy Ankem[1]

[1]Department of Materials Science & Engineering, University of Maryland, College Park, Maryland 20742

[2]Environmental Molecular Sciences Laboratory, Pacific Northwest National Laboratory, Richland, WA 99352

[*]Corresponding Author: Sarah Mburu

Address: Department of Materials Science and Engineering
2144 Chemical and Nuclear Engineering Building, #090
University of Maryland
College Park, MD 20742-2115, USA

E-mail: smburu@umd.edu

Phone Number: 301-405-7241

Fax Number: 301-405-6327

Abstract

The microstructure and mechanical properties in unaged and thermally aged (at 280 °C, 320 °C, 360 °C, and 400 °C to 4300 h) CF–3 and CF–8 cast duplex stainless steels (CDSS) are investigated. The unaged CF–8 steel has Cr-rich $M_{23}C_6$ carbides located at the δ–ferrite/γ–

austenite heterophase interfaces that were not observed in the CF–3 steel and this corresponds to a difference in mechanical properties. Both unaged steels exhibit incipient spinodal decomposition into Fe-rich *α*–domains and Cr-rich *α*'–domains. During aging, spinodal decomposition progresses and the mean wavelength (MW) and mean amplitude (MA) of the compositional fluctuations increase as a function of aging temperature. Additionally, G–phase precipitates form between the spinodal decomposition domains in CF–3 at 360 ^{o}C and 400 ^{o}C and in CF–8 at 400 ^{o}C. The microstructural evolution is correlated to changes in mechanical properties. (146 words)

Key Words: spinodal decomposition, duplex stainless steel, atom probe tomography, $M_{23}C_6$ carbide, G–phase

1. Introduction

Cast duplex stainless steels (CDSS) are used in cooling water pipes, valve bodies, pump casings, and elbows of light water nuclear reactors due to their high strength, ductility, weldability, castability, and excellent resistance to corrosion [1]. The properties of CDSS are due to their dual-phase (duplex) microstructure of body-centered cubic (b.c.c.) *δ*–ferrite and face-centered cubic (f.c.c.) *γ*–austenite phases [2] and [3]. The ferrite phase is present in volume percentages (fractions) that are typically between 9% and 15% in grades used in light water nuclear reactors, such as CF–3 and CF–8 stainless steels [1]. Despite desirable initial properties, these steels experience degradation of mechanical properties associated with thermal aging embrittlement during extended service at operational temperatures between 280 °C and 320 °C. Previous studies have reported that long-term thermal aging at operating temperature causes hardening, loss of impact toughness, and an increase in ultimate tensile strength (UTS) in these steels [1], [2], [4]–[15].

The need to extend the service life of light water nuclear reactors to 80 years from an initial design life of 40 years requires an assessment of the extent of thermal aging embrittlement of CDSS. Continuous temporal evolution of the microstructure accompanied by mechanical property degradation may prevent these steels from reaching an 80-year service life. However, performing thermal aging experiments over an 80 year cycle is impractical. An alternative approach is to perform accelerated aging experiments at higher temperatures that are kinetically similar to the operational temperatures (280 °C – 320 °C). Many studies have been performed at temperatures greater than 400 °C to accelerate the microstructural aging process and are summarized in Ref. [1]. However, the physical mechanisms leading to embrittlement can vary depending on aging temperature, which can complicate the ability to make relevant comparisons from accelerated aging experiments. For example, while it is generally accepted that phase decomposition does not occur in the f.c.c. γ–austenite phase [12], the embrittlement process is known to involve spinodal decomposition of the b.c.c. δ–ferrite phase [16] at temperatures < 400 °C, where the phase decomposes into Fe-rich α–phase domains and Cr-rich α'–phase domains. Whereas at temperatures > 400 °C, embrittlement is caused by the formation of the brittle σ–phase [1], [6], [10], [16]. However, the validity of using 400 °C as an accelerated aging temperature in CDSS has been questioned due to potentially different phase decomposition kinetics and embrittlement mechanisms when compared to operational aging temperatures [1], [5], [7], [11], [17], and [18]. Besides differences caused by aging temperature, the spinodal decomposition kinetics and amount of mechanical property degradation between steels can differ depending on their composition.

In addition to spinodal decomposition, other phases such as the G–phase and $M_{23}C_6$ carbide can form, which further complicates analysis. The G–phase, an intermetallic nickel silicide, is known to precipitate in the ferrite phase during thermal aging. A few early studies observed G–phase precipitates in CF–8 steel but examined the steel only after aging for many years [5], [15], [19]. Some recent studies evaluated G–phase precipitate evolution in CF–3M steel, which has high molybdenum (Mo) concentration, at temperatures greater than operational temperatures [12], [20], [21], and [22]. Since G–phase precipitation at operational temperatures between 280 °C and 320 °C is not well studied in some CDSS and there exists only limited evaluation of structure-property relationship, further investigation is required. The $M_{23}C_6$ carbide phase has been observed in some CDSS with high carbon (C) concentrations. Although the $M_{23}C_6$ carbide was observed after aging for long time periods at temperatures $\geq$ 400 °C [5], [7], and [11], Chung and Leax [11] suggested that the carbide phase may be present in the unaged state of these steels. However there have been no conclusive studies to confirm this and further investigation is required. Additionally, a recent CALculation of PHAse Diagrams (CALPHAD) study indicated that the $M_{23}C_6$ carbide phase is a thermodynamically stable phase at operational temperatures [16]. Currently, the evolution and influence that these intermetallic and carbide phases have on the degradation of mechanical properties is poorly understood, and is thus the focus of the study here. Despite the aforementioned studies, less attention has been paid to the unaged steels and operational temperatures. Furthermore, microstructural evolution and mechanical property degradation differences between CF–3 and CF–8 at operational and accelerated temperatures are not well addressed.

In the investigation described here, we characterize the mechanical properties and microstructure of CF–3 and CF–8 CDSS in both an unaged state and thermally aged for 4300 h at operational temperatures of 280 °C and 320 °C, and accelerated aging temperatures of 360 °C and 400 °C. We characterize and discuss the Cr-rich $M_{23}C_6$ carbide phase that is present in the unaged CF–8 steel by atom probe tomography (APT) and transmission electron microscopy (TEM). In contrast, we did not observe the Cr-rich $M_{23}C_6$ carbide phase in the unaged CF–3 steel. The sub-nanometer spatial resolution and high elemental sensitivity of the APT technique permits three-dimensional (3D) visualization of internal features [23]and [24], while TEM permits a wider field-of-view (FOV) than APT and acquisition of crystal structure information. We also assess the influence of the local Cr concentration on phase decomposition within the ferrite phase. We evaluate differences in the early stages of spinodal decomposition between the steels using APT. We measure amplitude and wavelength of concentration fluctuations in the ferrite phase that are consistent with the Cahn–Hilliard theory of spinodal decomposition [25], [26], and compare it to values of wavelength determined by the auto-correlation function (ACF) method [27] and amplitude determined by the Langer-Bar-on-Miller (LBM) method [28]. In general, we characterize the differences in phase decomposition – including spinodal domains and the G–phase in CF–3 and CF–8 when aging at different temperatures, and relate these results to mechanical property degradation of the two steels.

2. Experimental Procedures

2.1. Materials

The steels investigated in this study were obtained from Monett Company, Inc. as 17.8 cm × 3.3 cm × 2.9 cm rectangular keel blocks that were cast to the CF–3 and CF–8 standard specification outlined by ASTM A351-12b. All blocks of each steel type were cast from the same melt followed by a solution treatment at 1065 °C (1338 K) for 2 h and quenched in water at room temperature in accordance with the ASTM standard. The nominal chemical composition of the two steels as measured by optical emission spectroscopy (OES) is provided in Table 1. The keel blocks were mechanically reduced into 1.6 cm × 1.6 cm × 5.8 cm Charpy V-notch (CVN) and 1.6 cm × 1.6 cm × 8.9 cm tensile specimen blanks. The blanks were thermally aged in air to 4300 h in four Thermolyne™ Benchtop Muffle Furnaces at temperatures of 280 °C, 320 °C, 360 °C, and 400 °C. Subsequently, the blanks were computer numerical control (CNC) machined into test specimens in accordance with the ASTM standard procedures, as described below.

2.2. Mechanical Properties

2.2.1. *Charpy V-notch (CVN) Impact Toughness*

The CVN specimens were fabricated in accordance with the ASTM E23-12c standard from the specimen blanks. The 55 mm × 10 mm × 10 mm CVN specimens were tested employing a Tinius Olsen IT406 test frame at room temperature following the ASTM standard test procedures. The absorbed impact energy was measured and fracture morphology was observed for each specimen. The average of two or three measurements was reported for each aging condition, and the reported errors were based on the standard error of the mean.

2.2.2. Vickers Microhardness

Specimen blanks were mechanically reduced and cold mounted in epoxy for metallographic specimen preparation. The mounted specimens were ground and polished to 0.3 μm surface finish employing standard procedures. The polished specimens were tested using an Instron Tukon 2100 tester with a Vickers microhardness indenter, a load of 500 g, and dwell time of 15 s in accordance with the ASTM E384-11 standard procedures. The average of ten measurements was reported and the ± 2σ errors were based on the standard error of the mean.

2.2.3. Tensile Test

Cylindrical test specimens with a gauge diameter of 6.35 mm and a gauge length of 25.4 mm were fabricated in accordance with the ASTM E8-13a standard. Tensile tests were performed employing an Instron 8502 test frame equipped with an 8800 controller in accordance with the ASTM standard procedure. A preload of ~100 N was applied before the start of each test and a calibrated extensometer with 50% elongation capability was used for continuous measurement of strain using strain-rate control rate of 0.00025 s^{-1}. The extensometer was removed at its elongation limit and the tensile specimens were tested to failure using crosshead speed control rate of 0.006125 mm s^{-1} while measuring load and displacement. The ultimate tensile strength (UTS) was determined following the procedures outlined in the ASTM standard procedure.

2.3. Optical and Electron Microscopy

Optical microscopy was performed employing a Buehler® ViewMet Inverted Metallograph. The metallographic specimens were etched with Kalling's reagent No. 1 following standard procedures at room temperature to reveal the dual-phase microstructure.

Scanning electron microscope/focused ion beam (SEM/FIB) observations were performed employing a FEI Helios Nanolab 600 dual-beam instrument at 5 keV.

Transmission electron microscope (TEM) specimens for both unaged CF–3 and CF–8 steels were prepared by mechanical thinning to a thickness of approximately 200 μm before punch-out of 3 mm diameter foils. The foils were single-jet electropolished in 10 vol.% perchloric acid ($HClO_4$) solution in acetic acid (CH_3COOH) at 0 °C and 20 V for 10 minutes. The foils were then subsequently ion-beam milled at a 10° milling angle, 5 kV, and 3 mA until perforation in a Fischione Model 1010 milling system. The δ–ferrite/γ–austenite heterophase interfaces were observed by a JEOL 2100 LaB_6 TEM instrument operated at 200 kV and a JEOL 2100 field emission gun (FEG) TEM instrument operated at 200 kV equipped with an Oxford INCA 250 X-ray energy dispersive spectrometer (EDS). The selected area electron diffraction (SAED) technique was used to identify the δ–ferrite, γ–austenite, and $M_{23}C_6$ carbide phases in the foils. The TEM images and SAED patterns were analyzed using the Gatan Digital Micrograph Microscopy Suite software.

2.4. Atom Probe Tomography (APT)

2.4.1. Atom Probe Tomography Specimen Preparation

Specimens with a needle-shaped geometry necessary for APT analysis were fabricated using a FEI Helios Nanolab 600 dual-beam SEM/FIB instrument following standard lift-out and sharpening procedures [29], [30]. The *in situ* site-specific specimen preparation technique was performed on the metallographic mounts to take APT specimen blanks from δ–ferrite/γ–austenite heterophase interfaces, Figs. 1(a) – (b). To create the needle-shaped morphology necessary for APT analysis, annular milling was performed employing a 30 keV gallium ion (Ga^+) ion beam and sequentially decreasing probe currents following standard procedures after transfer of the region of interest (ROI) to the silicon (Si) microtip post with an Omniprobe micromanipulator, Figs. 1(c) – (e) [31]. As a final step, a low keV ion beam of 2 keV was allowed to raster over the specimen tip to remove material that had been damaged by the 30 keV Ga^+ ion beam annular milling operation [30]. The final apex of the specimen tips, imaged by SEM using 5 keV, had radii of ≤ ~50 nm suitable for APT analysis.

2.4.2. Atom Probe Tomography Data Acquisition, Reconstruction, and Data Analysis

A CAMECA Local-Electrode Atom Probe (LEAP®) 4000X instrument in the HR configuration, equipped with a reflectron for high mass resolution, was used for APT analysis. The specimen tip base temperature during data acquisition was set at 40 K. A voltage pulsed mode was applied to the specimen tips with a pulse-to-standing DC voltage ratio of between 15% and 20% at a pulse frequency of 200 kHz to promote field evaporation. The evaporation rate was maintained at a constant 1.5% rate or 0.015 ions per pulse. The background pressure was ~1.6×10^{-11} Torr (2.1×10^{-9} Pa). In order to precisely determine the time-of-flight (TOF) of the ions and thus their mass-to-charge state (*m*/*n*) ratios, we confirmed that the aforementioned pulse fraction range resulted in a lower probability of tip fracture, low background noise signal, and low incidences of multiple hits. Data sets of greater than four million ions were collected for each specimen tip, which corresponds to analysis depths of 60 nm to 120 nm depending on the tip radius. Data reconstruction and analysis were performed using the CAMECA Integrated Visualization and Analysis Software (IVAS), version 3.6.8. The APT specimen tips were reconstructed with a radius evolution defined using the tip profile morphology from SEM micrographs taken before APT analysis. Overlapping iron (Fe) and chromium (Cr) mass peaks at an *m*/*n* ratio of 54 were deconvoluted based on isotopic abundances.

The δ–ferrite/γ–austenite heterophase interfaces were delineated by a 4.5 at.% nickel (Ni) isoconcentration surface and associated proximity histogram concentration profiles [32] were used for compositional analysis [33]. The ± 2σ error bars were derived from counting statistics. The δ–ferrite phase and γ–austenite phase compositions were derived from the ion counts using only the plateau points [33] at a far-field distance of between 5 nm and 10 nm from the heterophase interfaces with ± $2\sigma \leq 0.25$ at.%. An analysis was performed to isolate the $M_{23}C_6$ carbide phase in the CF–8 steel and determine its composition using a 1 nm × 1 nm × 30 nm rectangular ROI and associated one-dimensional (1D) concentration profile. A small cross-section was chosen for the ROI in order to determine the core concentration of the carbide phase.

For spinodal decomposition analysis, a rectangular ROI of dimensions 3.2 nm × 3.2 nm × 30 nm was created in the ferrite phase of each unaged steel. The ROI was positioned at a distance of at least 1 nm away from the heterophase interfaces. The Fe (blue) and Cr (magenta) concentration profiles were determined using a fixed bin width of 0.2 nm. The initial concentration profile data was smoothed using a triangular 3-point moving average defined by $T_i = \frac{1}{4}(t_{i-2} + 2t_{i-1} + t_i)$ for bins $i \geq 3$, where t_i is the initial data set and T_i is the smoothed data set. The smoothed profiles were plotted with the mean of the Fe and Cr concentration profiles, which were derived from the ion counts in each bin, Figs. 2(a) – (b). The ± 2σ error bars of the mean Fe and Cr concentrations were derived from counting statistics. The alternating Fe and Cr concentration fluctuations were defined in the same method. A Cr concentration fluctuation was defined as when the concentration was greater than its mean value $+2\sigma$ and concomitantly the Fe concentration fluctuation was less than its mean value. Similarly, the Fe concentration fluctuation was defined as when its concentration was greater than its mean value $+2\sigma$ and concomitantly the Cr concentration fluctuation was less than its mean value. Thus, the periodic alternating fluctuations are defined along the ROI. We consider here that the amplitude of a concentration fluctuation, *A*, of Fe or Cr was defined as the highest point from the mean concentration value of that element, $A_j^k = C_j^k(max) - \bar{C}_j$, where *j* is the element and *k* is the peak number. The wavelength, λ, of Fe or Cr was defined as the distance between two adjacent amplitudes of a concentration fluctuation, $\lambda_j^k = x_j^{k+1} - x_j^k$, where *x* is the distance along the concentration profile, *j* is the element, and *k* is the peak number. The methodology discussed above is consistent with evaluation of wavelength and amplitude for periodic concentration fluctuations, and extant methods evaluate these quantities independently [34]. The above analysis was repeated using 20 non-overlapping rectangular ROIs in order to determine wavelength and amplitude size distributions. The wavelength (in nm) and amplitude (in at.%) size distribution histograms were plotted with a bin size of 0.5 for the ferrite phase of both the CF–3 and CF–8 steels. The mean wavelength (MW) and the mean amplitude (MA) were derived from the histograms. Deviation of the ROI cross-sectional dimension within a certain range did not significantly affect the wavelength and amplitude size distributions, thereby indicating a numerically stable evaluation procedure. Binomial distribution functions, which represent the distribution of random wavelengths and amplitudes, were superimposed on the histograms for comparative analysis. The mean wavelength results were compared with those obtained using the ACF method [27] using a bin size of 0.2 nm and the same rectangular ROI's. The mean amplitude results were compared with those determined by the LBM method [28] using a bin (block) size of 100 atoms and the same rectangular ROI's.

The G–phase precipitates in the APT reconstructions were delineated by 6.5 at.% Ni isoconcentration surfaces. The precipitate volume equivalent sphere radii, <*R*> [33], number density, N_V, volume percentage (fraction), V_f, and core compositions are reported. The estimated steel density, ρ, is 8.46×10^{22} atoms cm^{-3}, which was used to calculate the reconstructed volumes of the APT specimen tips [33] and the estimated detection efficiency, η, is 36% for this atom probe instrument. The G–phase core compositions were derived from the four data points on the right hand side of the proxigram concentration profiles. Deviations of the isoconcentration surface threshold value within a certain concentration range did not significantly change the number of detected precipitates or their proxigrams thereby indicating a numerically stable evaluation procedure.

3. Results and Discussion

3.1. Mechanical Properties

3.1.1. Vickers Microhardness

The results in Fig. 3(a) illustrate that the unaged CF–3 has a lower mean Vickers microhardness value of 151.8 ± 4.6 HV500g, whereas the unaged CF–8 in Fig. 3(d) has a greater mean value of 165.8 ± 5.8 HV500g. As we discuss below, this difference is possibly caused by the presence of the $M_{23}C_6$ carbide phase at the heterophase interfaces in the CF–8 steel but not the CF–3 steel. Additionally, C is well known to cause interstitial solid-solution hardening and the nominal concentration of C in the CF–8 steel is greater than in the CF–3 steel. The mean Vickers microhardness increased for both steels after aging to 4300 h due to phase decomposition, as discussed below. The rates of microhardness increase, as indicated by the slopes of the trend lines in Figs. 3(a) and 3(d) is approximately twice as great at the accelerated temperatures than at the operational temperatures. The slopes are greater for the CF–3 steel than the CF–8 steel in general indicating that the microhardness increases faster for CF–3. However, after aging, the microhardness values of the two steels are comparable at all four temperatures. The mean microhardness values are greater after aging at accelerated temperatures than operational temperatures for both steels.

3.1.2. Tensile Properties

The unaged CF–3 steel has a UTS value of 530 MPa, in Fig. 3(b), and the unaged CF–8 steel has a UTS of 570 MPa, Fig. 3(e). The higher strengths in the CF–8 steel may possibly be due to the presence of the $M_{23}C_6$ carbide phase at the heterophase interfaces. The higher Vickers microhardness and UTS values are consistent with the $M_{23}C_6$ carbide phase acting to strengthen the unaged CF–8 steel when compared to the unaged CF–3 steel. This result is similar to that of Mathew, et al. [35], who reported a UTS of ~600 MPa for a CF–8 steel. Additionally, Michaud, et al. [36] performed tensile property characterization of CF–3 and CF–8 steels and reported a UTS of ~390 MPa for CF–3 steel, while the CF–8 steel exhibited a UTS of ~525 MPa. The trend is consistent with the steels in this study, where CF–8 steel has higher UTS than the CF–3 steel. The mean UTS increased for both steels after aging to 4300 h at the accelerated temperatures and the values were similar between the steels. A difference in behavior was observed when aging at the two operational temperatures. The mean UTS increased for both steels when aging at 320 °C but it only increased for CF–8 and not CF–3 when aging at 280 °C. Furthermore, a difference in mean UTS values still existed between the two steels, unlike when aging at accelerated temperatures. The rates of UTS increase, as indicated by the slopes of the trend lines in Figs. 3(b) and 3(e) is more than twice as great at the accelerated temperatures than at the operational temperatures. The slopes are greater for the CF–3 steel than the CF–8 steel in general indicating that the UTS increases faster for the CF–3. However, the mean UTS values were greater after aging at accelerated temperatures than operational temperatures.

3.1.3. Charpy V-notch Impact Toughness (CVN)

As illustrated in Fig. 3(f), the lower CVN impact toughness value of the unaged CF–8 of 317 ± 80 J as compared to the unaged CF–3 of 392 ± 14 J in Fig. 3(c) is most likely due to the presence of $M_{23}C_6$ carbides at the heterophase interfaces. Carbides located at the heterophase interfaces may influence the failure mode by causing phase boundary separation thereby leading to low impact toughness values [13]. Previous research also demonstrated a similar trend where an as-cast CF–3 steel [8] had a higher upper shelf energy of > 300 J when compared to the unaged CF–8 steel [19], which had an upper shelf energy of 225 J. The mean CVN values decreased for both steels after aging to 4300 h at all four temperatures and the mean values were similar between the steels at the accelerated temperatures. At operational temperatures, the CF–8 steel exhibited a greater reduction in mean CVN values when compared to CF–3. Furthermore, a difference in mean CVN values still existed between the two steels unlike when aging at accelerated temperatures. The mean CVN values were lower after aging at accelerated temperatures than operational temperatures and both steels exhibited the lowest CVN value when aging at 400 °C. The unaged specimens exhibited ductile fracture with significant deformation and did not completely break. All aged specimens exhibited more brittle fracture with less deformation and more granular fracture surfaces. The rates of impact toughness decrease, as indicated by the slopes of the trend lines in Figs. 3(c) and 3(f) is more than twice as great at the accelerated temperatures than at the operational temperatures. The slopes are greater for the CF–3 steel than the CF–8 steel indicating that the impact toughness decreases faster in CF–3.

3.2. Microstructural Characterization

3.2.1. Optical Microscopy: Microstructure

An optical micrograph, Fig. 4, illustrates a microstructure consisting of a network of island-shaped δ–ferrite phase (dark color) in the continuous γ–austenite phase (light color) for the unaged CF–3 steel. The microstructure of the unaged CF–8 steel has a qualitatively similar appearance to that of the CF–3 steel. The ferrite volume percentage is 11.5 ± 1.1 % for the CF–3 steel while that of the CF–8 steel is 9.1 ± 0.9 % as measured by the manual point counting method specified in the ASTM E562-11 standard [37] and [38]. The microstructure observed in this study is consistent with that reported in the literature of a steel with a composition similar to CF–8 and with a ferrite volume percentage of less than 20 % [39], [40]. The ferrite volume percentage remained approximately constant when aging to 4300 h at all four temperatures.

3.2.2. Atom Probe Tomography (APT) and Transmission Electron Microscopy (TEM): $M_{23}C_6$ Carbide at the Heterophase Interfaces

The proximity histogram (proxigram) concentration profiles across the δ–ferrite/γ–austenite heterophase interfaces are qualitatively similar for the unaged CF–3 and CF–8 steels, Figs. 5(a) – (b) and 6(a) – (b), respectively. However a distinct carbide phase is observed in the CF–8 reconstruction, Fig. 6(a). The peak C concentration at the heterophase interface is ~0.8 at.% for the CF–3 steel and ~1.5 at.% for the CF–8 steel, which is influenced by the presence of a carbide phase. As discussed below, this carbide phase is identified as the $M_{23}C_6$ carbide. Since the CF–8 steel has a greater nominal C concentration than the CF–3 steel, the thermodynamic driving force for carbide formation at the heterophase interfaces is greater [16]. A more detailed analysis, Figs. 7(a) – (d), was performed to determine the $M_{23}C_6$ carbide phase composition. The carbides are interspersed along the δ–ferrite/γ–austenite heterophase interface of the APT specimen tip, Fig. 7(a), and an example carbide is visible in the APT reconstructions, Figs. 7(b) –

(c). The Cr and C are enriched, while Fe and Ni are depleted within the carbide phase (black box) relative to the austenite phase, Fig. 7(d). The carbide composition is 32.5 $\pm$ 2.1 at.% Fe, 49.2 $\pm$ 1.5 at.% Cr, 11.9 $\pm$ 1.2 at.% C, 2.0 $\pm$ 0.4 at.% Mo, 2.1 $\pm$ 0.7 at.% Ni, 1.1 $\pm$ 0.2 at.% Mn, and 0.65 $\pm$ 0.14 at.% Si. Recent CALPHAD calculations indicate that the most common carbide present in CF–8 steels is the f.c.c. $M_{23}C_6$ carbide, where M = Cr [16]. Since the steels were cast, solution-treated, and quenched in water at room temperature, the carbide composition in the unaged state is most likely not yet at equilibrium.

The δ–ferrite/γ–austenite heterophase interfaces in both unaged steels were also observed by conventional TEM. The interfaces of the unaged CF–3 steel were consistently straight and uniform and did not exhibit a carbide phase as demonstrated by the lack of superlattice reflection spots in the SAED pattern, Fig. 8(a) inset. Carbides were also not observed in the b.c.c. δ–ferrite phase or the f.c.c. γ–austenite phase grains at locations away from the heterophase interfaces. The lack of carbides in the microstructure is most likely due to the low nominal C concentration, Table 1. In contradistinction, the interfaces in the CF–8 steel were noticeably more undulating than in the CF–3 steel, Fig. 8(b), and SAED patterns taken at the interfaces along the [001], Fig. 8(b) inset, and $[\bar{3}01]$, Fig. 9(c), γ–austenite zone axes reveal the presence of f.c.c. superlattice diffraction spots indicative of an $M_{23}C_6$ carbide phase. These spots are not, however, present in the SAED patterns at the interior of either the δ–ferrite phase or γ–austenite phase grains. Additionally, the $M_{23}C_6$ carbide and γ–austenite phase exhibit a cube–cube orientation relationship (OR) of $\{111\}_\gamma \| \{333\}_{M_{23}C_6}$, $\langle 110\rangle_\gamma \| \langle 330\rangle_{M_{23}C_6}$. The $M_{23}C_6$ carbide has an elongated morphology, Figs. 9(a) – (b), with a length of ~230 nm and width of ~90 nm. Other carbides of the same type were observed at multiple different heterophase interfaces in CF–8, and exhibit a morphology similar to the one illustrated in Figs. 9(a) – (b). The lattice parameter,

a, was measured as 1.109 nm in this study, which is slightly greater than the experimental value of $a = 1.065$ nm reported by Southwick and Honeycombe in a different DSS [41]. It is also similar to other values reported in the literature of approximately between 1.05 nm and 1.10 nm [42], [43]. The lattice parameter is known to exhibit small variations due to differences in chemical composition [38]–[40].

A TEM-EDS line-scan was taken from the interior of the δ–ferrite phase grain across an $M_{23}C_6$ carbide and ending in the interior of the γ–austenite phase grain, Fig. 9(d). The results illustrate that the carbide is enriched in Cr and C, and contains smaller quantities of Mn, Ni, Mo, and Si. The carbide is depleted in Fe and Ni when compared to the adjacent ferrite and austenite phases. Furthermore, a depletion of Cr in the b.c.c. δ–ferrite phase is observed up to a distance of approximately 50 nm away from the heterophase interface, which suggests the presence of a solute depleted zone (SDZ). These observations support the APT observations that the $M_{23}C_6$ carbide contains metallic elements other than Cr. Additionally, earlier STEM-EDS observations in a different steel containing a smaller nominal concentration of 2.6 wt.% Cr also indicated that $M_{23}C_6$ carbides contain metallic elements other than Cr [44]. Recent first principles calculations of a model ternary alloy also illustrate that Fe can substitute on the Cr lattice forming a $Cr_{23-x}Fe_xC_6$ carbide [42].

The occurrence of the SDZ in the ferrite phase of CF–8 and not CF–3 suggests that the Cr-rich carbides locally influence the phases' composition. Additionally, the SDZ formation in the ferrite phase and not the austenite phase suggests that differences in Cr diffusivity in each phase also influence its formation. Since Cr is the predominant metallic element in the $M_{23}C_6$ carbide [45], its nonstoichiometric composition in the unaged CF–8 suggests that Cr diffuses into the carbide during aging while Fe, Mo, Ni, Mn, and Si most likely diffuse into the surrounding matrix phases thereby permitting its composition to approach equilibrium. In addition, since the $M_{23}C_6$ carbide is located at the heterophase interface, enhanced or short circuit diffusion of Cr from the ferrite phase into the carbide phase along the interface may occur. The diffusion of solute elements at grain boundaries and heterophase interfaces can be several orders of magnitude greater than in the bulk volume [46], [47], and the formation of the SDZ in the ferrite phase of the unaged CF–8 suggests that the kinetics are fastest at the heterophase interface. The influence of the $M_{23}C_6$ carbide on the local Cr concentration at the heterophase interface and formation of an SDZ in the ferrite phase of CF–8 but not CF–3 is supported by APT observations where we measure a mean Cr concentration of 24.9 at.% for CF–8, Fig. 6(b), and 28.7 at.% in the ferrite phase for CF–3, Fig. 5(b). The mean Cr concentration is 22.3 at.% in the austenite phase of both steels. Hence, formation of the carbide locally depletes the Cr concentration in the ferrite phase of CF–8. A similar SDZ was observed at a grain boundary (GB) in a multicomponent Fe-Cu steel due to the presence of an Fe_3C carbide at the interface and was also attributed to more rapid kinetics [48].

We now consider the differences in diffusivity of Cr between the two phases. Williams and Faulkner studied Cr diffusion in ferritic and austenitic steels [49] and found that Cr in b.c.c. ferrite had a diffusion constant of $D_o = 0.15\left(\frac{+0.54}{-0.12}\right)\ \mathrm{cm^2 s^{-1}}$ and activation energy of $Q = 210(\pm 15)\ \mathrm{kJ\ mol^{-1}}$, whereas Cr in f.c.c. austenite had a diffusion constant of $D_o = 0.27\left(\frac{+1.04}{-0.22}\right)\ \mathrm{cm^2 s^{-1}}$ and $Q = 264(\pm 16)\ \mathrm{kJ\ mol^{-1}}$. The Arrhenius diffusion equation of Cr is $\overline{D}_{Cr} = D_o e^{-Q/RT}$, where R is the gas constant 8.31 J $(\mathrm{mol\ K})^{-1}$ and T is the absolute temperature. The diffusion distance during solution treatment can be determined to a first order approximation using the solution treatment temperature of 1338 K (1065 °C). The 3D root-mean-square (RMS) diffusion distance of Cr, $\langle x_{Cr}\rangle = \sqrt{6 \times \overline{D}_{Cr} \times t}$, is 64.1 μm in ferrite, and

7.6 μm in austenite where t is the solution treatment time of 7200 s. Thus, Cr has a diffusion distance in the ferrite phase an order of magnitude greater than in the austenite phase for the same time interval indicating that the Cr diffusion kinetics are more rapid in ferrite thereby promoting the formation of a Cr SDZ at the interface.

The aforementioned results demonstrate that the lower impact toughness, higher UTS, and higher Vickers microhardness observed in the unaged CF–8 steel are likely due to the presence of the carbides at the heterophase interfaces. Carbides were also observed at the heterophase interfaces of CF–8 steels aged to 4300 h. We do not, however, observe $M_{23}C_6$ carbides in CF–3 in the unaged condition or after aging to 4300 h at either operational or accelerated temperatures. These observations are in contrast to those in Refs. [5], [7], and [11], which only observed the carbide phase in CF–8 aged at ≥ 400 °C. Thus, some studies have suggested that care must be taken in using 400 °C as an accelerated temperature in CF–8, as it may not be representative of aging at operational temperatures. Our observations suggest, however, that contribution to embrittlement in CF–8 by the $M_{23}C_6$ carbide can occur at both operational and accelerated aging temperatures since the carbide is present following solidification and solution treatment. It has been previously shown that the $M_{23}C_6$ carbide phase can form at the δ–ferrite/γ–austenite heterophase interfaces during the austenite-to-ferrite transformation in steels [50] and [51], and hence its presence can reasonably be expected in the unaged CF–8 steels, as has been observed here.

3.2.3. Atom Probe Tomography (APT): Spinodal Decomposition

Incipient spinodal decomposition as illustrated by concentration fluctuations in the ferrite phase of the unaged CF–8 stainless steel was observed, Figs. 2(a) – (b). The ferrite phase of the unaged CF–3 stainless steel also exhibited incipient spinodal decomposition that was qualitatively similar to that observed in the CF–8 steel. Spinodal decomposition in the CDSS is described as phase separation of the δ–ferrite phase into Fe-rich α–domains (blue) and Cr-rich α'–domains (magenta). Our observations are similar to those in unaged model Fe–25Cr at.%, Fe–30Cr at.%, and Fe–36Cr at.% binary alloys where the authors suggested that small amounts of decomposition may be present in the unaged ferrite phase due to the presence of positive Cr–Cr interactions at short distances when using radial distribution function (RDF) analysis [52]. Moreover, an earlier study by Pumphrey and Akhurst on an unaged CF–3 steel suggested that a small spinodal amplitude exists in the ferrite phase, but the wavelength was not determined [9]. Phase decomposition in the ferrite phase is seen to progress and the wavelength and amplitudes of the concentration fluctuations are observed to increase during aging to 4300 h as illustrated for the CF–8 steel at 400 °C, Figs. 10(a) – (b). Additionally, a small G–phase precipitate is observed at an α–domain/α'–domain interface in Fig. 10(a) and is discussed below. The increase in wavelength and amplitude occurs at the two operational and the two accelerated aging temperatures in both steels.

The Cr wavelength and amplitude size distributions in the unaged CF–3 and CF–8 stainless steels are illustrated in Figs. 11(a) – (b) and Figs. 11(c) – (d), respectively. The binomial distribution of random wavelengths and amplitudes are superimposed on both figures and differ from the experimentally measured distributions. The quantity MW for Cr in CF–3 is 1.9 ± 0.2 nm and 1.8 ± 0.2 nm in CF–8.The quantity MA for Cr in the CF–3 steel is 4.4 ± 0.2 nm and 4.4 ± 0.2 nm in the CF–8 steel. The MW values are slightly different than the mean wavelength determined by the ACF method, whereas the MA values exhibit greater difference with the amplitude determined by the LBM method, Figs. 12(a) – (b).

In order to account for the measured differences in local mean Cr concentration in the b.c.c. δ–ferrite phase on the Cr spinodal decomposition amplitudes between the CF–3 and CF–8 steels, a ratio of normalized spinodal decomposition amplitudes, A_j^*, was calculated for an element j, $A_j^* = |A_i^{CF-8}|/|A_i^{CF-3}| = \{(A_j^{CF-8} / \bar{C}_j^{CF-8})\}/\{A_j^{CF-3} / \bar{C}_j^{CF-3}\}$. The mean concentrations used in the equation for the quantity A_j^* are from the proxigrams in Figs. 5(b) and 6(b) for CF–3 and CF–8, respectively. The quantity A_j^* for Cr is 1.15, which indicates the normalized Cr amplitude is greater in the CF–8 steel. A decrease of the local mean Cr concentration in the ferrite phase may affect the Cr atomic mobility due to the concentration dependence of the interdiffusion coefficient [53], [54] in the Cahn–Hilliard equations and thus lead to different spinodal decomposition amplitudes in the steels. The small differences in nominal composition between the two steels suggest that incipient spinodal decomposition should be similar since the two steels would have a similar position in the miscibility gap of the phase diagram and hence the driving force for phase separation would be similar. The APT results demonstrate, however, that the normalized Cr amplitude in the unaged CF–8 steel is greater than in the CF–3 steel. This is possibly due to the presence of the Cr-rich $M_{23}C_6$ carbide phase in CF–8 and not CF–3 that locally influences the Cr concentration in the ferrite phase by formation of the SDZ, as discussed above. In addition to the direct influence of the carbide phase on the measured differences in mechanical properties of the unaged steels, it is possible that the carbide also indirectly influences thermal embrittlement by affecting the Cr concentrations and amount of spinodal decomposition in the ferrite phase. The smaller differences in mechanical properties between the steels after aging to 4300 hours at accelerated temperatures when compared to operational temperatures suggest, however, that this effect may be limited to earlier stages of decomposition.

After aging to 4300 h, the quantities MW and MA for Cr derived from wavelength and amplitude size distributions increase as illustrated in Figs. 12(a) – (f). The quantities MW and MA exhibit an increasing trend with increasing aging temperature and their values are greater for both accelerated temperatures when compared to the two operational temperatures for both steels. Additionally, only small differences are exhibited in the quantities MW and MA between the two steels at operational temperatures. The difference in values of these quantities, are however, slightly greater at accelerated temperatures and this may be caused by the influence of the G–phase precipitates on spinodal decomposition, as discussed below. The quantity MW exhibits slight differences when compared to the mean wavelength determined by the ACF method but both methods illustrate similar trends. The amplitude determined by the LBM method is consistently greater than when compared to the quantity MA but both values exhibit similar trends. Earlier studies of evaluating spinodal decomposition have illustrated quantitative differences between various methods of determining amplitude although they may exhibit similar trends [28] and [52]. In this study, the differences observed between the LBM method and the quantity MA is due to their underlying basis. The LBM method is categorized as a peak-to-trough amplitude method, whereas the method presented in this study is a peak-to-mean composition amplitude method and thus the former will have quantitative values approximately twice as great as the latter. Furthermore, the LBM method is dependent on symmetry of the frequency distributions [52], and multicomponent alloys whose nominal or local compositions are not centered in the miscibility gap of the phase diagram, such as the CF–3 and CF–8 CDSS in this study, will exhibit asymmetry and thus the LBM method can produce greater variability in its results.

3.2.4. Atom Probe Tomography (APT): G–phase Precipitates

G–phase precipitates were not observed in the unaged specimens or the specimens aged at operational temperatures in both steels, as illustrated in Figs. 13(a) – (b). G–phase precipitates are detected inside the decomposing ferrite phase of CF–3 aged at 360 °C and 400 °C, and CF–8 aged at 400 °C. The G–phase is observed to form at the α/α' interfaces as illustrated in Figs. 10(a) – (b). The G–phase is a ternary intermetallic silicide that has a nominal stoichiometric composition of $Ni_{16}Si_7Ti_6$ [55]. However, other metallic elements such as Cr, Fe, and Mn can substitute for Ni and titanium (Ti) [6], [55], and [56]. As depicted in the example proxigram concentration profiles of CF–8 aged at 400 °C in Fig. 14, the G–phase precipitates are enriched in Ni, Si, Mn, and Cu but are depleted in Fe, Cr, and Mo and their compositional analysis is reported in Table 2. Copper is present as a residual element in the steels. The precipitates still contain measurable concentrations of Fe and Cr after aging to 4300 h. It is possible that both elements diffuse out of the G–phase while Ni, Si, and Mn diffuse into the G–phase during further aging and the precipitates approach their equilibrium compositions. This is supported by the lower Fe and Cr concentrations and concomitantly higher Ni, Si, and Mn concentrations at 400 °C aging when compared to the slower kinetics at 360 °C aging for the CF–3 steel. Trajectory aberrations and local magnifications effects may also influence the Fe and Cr concentrations in the G–phase. However, since the quantity $<R>$ is > 1 nm, this will have limited effect on the core compositions [57]. Furthermore, recent studies of the G–phase in CF–3M illustrated that Fe and Cr concentrations decrease while Ni, Mn, Si, and Mo concentrations increase in the precipitates with increasing aging time at accelerated temperatures [12] and [21]. The quantities $<R>$, N_V, and V_f of the G–phase precipitates in CF–3 are greater than that of CF–8 when aging at 400 °C, Table 3, which suggests that the kinetics of G–phase formation are slower in the latter. Further, the same morphological parameters are greater when aging at 400 °C than 360 °C in CF–3 due to faster kinetics. Comparison of the precipitate radii, number density, and volume percentage results for CF–3 at 360 °C and 400 °C in this study to CF–3M at 350 °C and 400 °C in Ref. [21] suggests that the kinetics of G–phase formation is slower in CF–3. These differences can be accounted for by variations in nominal composition, solution treatment, and heterogeneous distribution of the G–phase precipitates. The CF–3M steel in Ref. [21] had a greater nominal concentration of Ni, which is known to accelerate G–phase formation, and a greater nominal concentration of Mo, which is also known to promote G–phase precipitation [7].

3.2.5. Comparison of Mechanical Property and Microstructural Evolution

In general, the increasing Vickers microhardness, increasing UTS, and decreasing CVN impact toughness in both steels as illustrated in Figs. 3(a) – (f) corresponds to increasing values for the quantities MW and MA in both steels as illustrated in Figs. 12(a) – (f). Additionally, the greater values for MW and MA at accelerated temperatures compared to operational temperatures correspond in general to the greater degradation of the mechanical properties at the accelerated temperatures. As discussed above, the extent of spinodal decomposition increases with increasing temperature. In addition to the contribution by spinodal decomposition, G–phase precipitation at accelerated temperatures may influence embrittlement but its contribution has been debated in the literature and is not completely clear. The G–phase was reported to contribute to embrittlement in Refs. [58], [59], and [60], whereas it was reported to have more limited contributions in Refs. [5], [11], and [12]. We measure little difference in the degree of mechanical property degradation at 360 °C aging between CF–3 with G–phase precipitation and CF–8 without G–phase precipitation thereby suggesting that its direct contribution is limited. It is possible, however that the G–phase could indirectly influence embrittlement by locally altering the Ni concentration, which would in turn influence kinetics of spinodal decomposition in the ferrite phase as suggested in Refs. [6] and [11].

5. Conclusion

The effect of aging temperatures on the mechanical property degradation and phase decomposition in CF–3 and CF–8 steels was studied experimentally. The *δ*–ferrite/*γ*–austenite heterophase interface, $M_{23}C_6$ carbide, spinodal decomposition, and G–phase precipitation were analyzed in unaged and aged steels. The steels were aged at operational temperatures of 280 °C and 320 °C and accelerated temperatures of 360 °C and 400 °C for 4300 h. This investigation resulted in the following findings:

(1) Compared to the unaged CF–3 steel, the unaged CF–8 steel has higher UTS and Vickers microhardness values, but lower CVN impact toughness values. The CF–3 steel has a UTS of 530 MPa, Vickers microhardness of 151.8 ± 4.6 HV500g, and impact toughness of 392 ± 14 J. The CF–8 steel has a UTS of 570 MPa, Vickers microhardness of 165.8 ± 5.8 HV500g, and impact toughness of 317 ± 80 J.

(2) Selected area electron diffraction (SAED) observations illustrated that a $M_{23}C_6$ carbide is present at the heterophase interphases of the unaged CF–8 steel but not the unaged CF–3 steel, and it is not present in the interior of the grains in either steel. The carbide phase is not observed in the CF–3 after aging to 4300 h. The $M_{23}C_6$ carbide has an f.c.c. crystal structure with a lattice parameter of 1.109 nm. It has a composition of 32.5 ± 2.1 at.% Fe, 49.2 ± 1.5 at.% Cr, 11.9 ± 1.2 at.% C, 2.0 ± 0.4 at.% Mo, 2.1 ± 0.7 at.% Ni, 1.1 ± 0.2 at.% Mn, and 0.65 ± 0.14 at.% Si. A Cr solute depleted zone (SDZ) is present in the ferrite phase of the unaged CF–8 but

not the unaged CF–3. In the ferrite phase, the Cr concentration was 28.7 at.% in the CF–3 steel and 24.9 at.% in the CF–8 steel with a carbide present at the heterophase interface.

(3) Incipient spinodal decomposition was observed in the b.c.c. δ–ferrite phase of the unaged CF–3 and CF–8 steels. The wavelength and amplitude size distributions differed from binomial distribution of random wavelengths and amplitudes. The spinodal domains in CF–3 steel have a mean wavelength (MW) of 1.8 $\pm$ 0.2 nm and a mean amplitude (MA) of 4.4 $\pm$ 0.2 at.% Cr, whereas the domains in CF–8 steel have a MW of 1.9 $\pm$ 0.2 nm and a MA of 4.4 $\pm$ 0.2 at.% Cr.

(4) After aging to 4300 h spinodal decomposition progresses and the quantities MW and MA increase for both steels at the two operational and two accelerated temperatures. These quantities are greater in the steels aged at accelerated temperatures than operational temperatures. Concomitantly, the Vickers microhardness and UTS increase while the CVN impact toughness values decrease for both steels. The mechanical property degradation is greater at accelerated temperatures than operational temperatures.

(5) G–phase precipitates were observed in CF–3 aged at 360 ^{o}C and both steels aged at 400 ^{o}C. The radius, number density, and volume percentage (fraction) of G–phase in CF–3 are greater than those in CF–8.The radius, number density, and volume percentage is 1.1 $\pm$ 0.4 nm, $9.5 \times 10^{22} \pm 4.1 \times 10^{22}$ $\mathrm{ppts./m^3}$, and 0.1 $\pm$ 0.02 %, respectively, for the CF–3 steel aged at 360 ^{o}C; and is 2.0 $\pm$ 0.2 nm, $1.7 \times 10^{23} \pm 4.3 \times 10^{22}$ $\mathrm{ppts./m^3}$, and 0.8 $\pm$ 0.02 %, respectively, for the CF–3 steel aged at 400 ^{o}C. The same parameters are 1.6 $\pm$ 0.3 nm, $1.3 \times 10^{23} \pm 3.3 \times 10^{22}$ $\mathrm{ppts./m^3}$, and 0.4 $\pm$ 0.02 %, respectively, in the CF–8 steel aged at 400 ^{o}C.

Acknowledgements

This work is supported by the Department of Energy – Nuclear Energy University Program (DOE–NEUP), contract number DE–NE0000724; Dr. Jeremy T. Busby, Oak Ridge National Laboratory (ORNL), technical monitor. A part of this research was performed using the Environmental Molecular Sciences Laboratory (EMSL), a DOE Office of Science User Facility sponsored by the Office of Biological and Environmental Research and located at Pacific Northwest National Laboratory (PNNL). We would like to thank Mr. Michael Perna, University of Maryland (UMD), for machining all specimen blanks and mechanical property test specimens; Professor Isabel Lloyd, UMD, for use of the Vickers microhardness tester; and Dr. Robert Bonenberger, UMD, for his assistance with the equipment in the Modern Engineering Materials Instructional Laboratory (MEMIL). Ms. Sarah Mburu is partially supported by the National Science Foundation (NSF) Louis Stokes Alliances for Minority Participation (LSAMP) under Grant No. 0833018. Mr. Schwarm would like to acknowledge the Department of Energy: Office of Nuclear Energy (DOE-NE) Integrated University Program (IUP) fellowship program for support. We acknowledge the support of the Maryland NanoCenter and its AIMLab and FabLab.

List of Tables

Table 1. Nominal composition (wt.%) of the CF–3 and CF–8 cast duplex stainless steels (CDSS) as measured by optical emission spectroscopy (OES).

Steel		Composition (wt.%)						
		Fe	Cr	Ni	Si_{max}	Mn_{max}	Mo_{max}	C_{max}
CF–3	**ASTM A351**	Balance	17.0–21.0	8.0–12.0	2.00	1.50	0.50	0.03
	Unaged	69.52	19.69	8.40	0.98	1.07	0.28	0.02
CF–8	**ASTM A351**	Balance	18.0–21.0	8.0–11.0	2.00	1.50	0.50	0.08
	Unaged	69.44	19.85	8.30	0.97	0.99	0.35	0.06

Table 2. Composition of G–phase precipitates in CF–3 and CF–8 after 4300 h aging as measured by atom probe tomography (APT).

		Composition (at.%)						
		Fe	**Cr**	**Ni**	**Si**	**Mn**	**Cu**	**Mo**
CF–3	**360 ^{o}C**	54.19	19.07	17.21	3.72	4.19	0.93	0.23
	400 ^{o}C	40.14	15.05	22.23	7.44	7.18	6.83	0.61
CF–8	**360 ^{o}C**	ND	ND	ND	ND	ND	ND	ND
	400 ^{o}C	45.60	13.88	20.39	7.21	7.58	4.14	0.23

ND = Not detected.

Table 3. Mean radius, <*R*>, number density, N_V, and volume percentage, V_f, of G–phase precipitates in CF–3 and CF–8 after 4300 h aging as measured by atom probe tomography (APT).

		Parameters		
		$\langle R \rangle$ (nm)	N_V (ppt./m^3)	V_f (%)
CF–3	**360 ^{o}C**	1.1 ± 0.4	$9.5 \times 10^{22} \pm 4.1 \times 10^{22}$	0.1 ± 0.02
	400 ^{o}C	2.0 ± 0.2	$1.7 \times 10^{23} \pm 4.3 \times 10^{22}$	0.8 ± 0.02
CF–8	**360 ^{o}C**	ND	ND	ND
	400 ^{o}C	1.6 ± 0.3	$1.3 \times 10^{23} \pm 3.3 \times 10^{22}$	0.4 ± 0.02

ND = Not detected.

List of Figure Captions

Graphical Abstract. Understanding relationships between microstructure and mechanical behavior in cast duplex stainless steels across multiple length scales.

Figure 1. (a) Site-specific lift-out of an APT specimen tip at an example *δ*–ferrite/*γ*–austenite heterophase interface (dashed yellow line) using a SEM/FIB instrument. (b) – (e) series of images illustrating the annular milling of a specimen into a needle morphology with sequentially decreasing tip diameter necessary for APT analysis.

Figure 2. (a) An example region of interest (ROI) illustrating the compositional heterogeneity of alternating Fe-rich *α*–domains (blue) and Cr-rich *α'*–domains (magenta) with (b) corresponding Fe and Cr concentration profiles. The individual fluctuation peaks in the Fe and Cr profiles are numbered and an example wavelength, *λ*, and amplitude, A, are depicted for the Fe profile. The mean of the Fe and Cr concentrations are superimposed in the plot as solid horizontal lines.

Figure 3. Mechanical properties as a function aging time at the unaged (green diamonds) and 280 °C (red circles), 320 °C (blue squares), 360 °C (purple triangles), and 400 °C (orange stars) aging temperatures: Vickers Microhardness of (a) CF–3 and (d) CF–8, ultimate tensile strength (UTS) of (b) CF–3 and (e) CF–8, and Charpy V-notch (CVN) impact toughness of (c) CF–3 and (f) CF–8. Solid symbols indicate CF–3 while open symbols indicate CF–8. Trend lines from the unaged data to the aged data are drawn with corresponding colors. The operational temperatures (280 °C and 320 °C) are solid lines, while the accelerated temperatures (360 °C and 400 °C) are dashed lines.

Figure 4. Optical micrograph of the unaged CF–3 stainless steel microstructure illustrating the *γ*–austenite phase (light color) and islands of *δ*–ferrite phase (dark color).

Figure 5. (a) APT reconstruction of unaged CF–3 with 61 nm × 64 nm dimensions illustrating the *δ*–ferrite/*γ*–austenite heterophase interface. 0% of the Fe (blue) ions, 30% of the Cr ions (magenta), and 100% of Ni (green), Mn (mustard), Si (gray), Mo (red), and C (black) are depicted for clarity. (b) Proximity histogram concentration profiles for Fe (blue circles), Ni (green squares), Mn (mustard stars), Cr (magenta triangles), Si (gray diamonds), Mo (red asterisks), and C (black left–triangles) using a 4.5 at.% Ni isoconcentration surface. The $\pm 2\sigma$ error bars are based on counting statistics. For the major elements, the error bars are smaller than the marker size.

Figure 6. (a) APT reconstruction of unaged CF–8 with 94 nm × 61 nm dimensions illustrating the *δ*–ferrite/*γ*–austenite heterophase interface. 0% of the Fe (blue) ions, 30% of the Cr ions (magenta), and 100% of Ni (green), Mn (mustard), Si (gray), Mo (red), and C (black) are depicted for clarity. (b) Proximity histogram concentration profiles for Fe (blue circles), Ni (green squares), Mn (mustard stars), Cr (magenta triangles), Si (gray diamonds), Mo (red asterisks), and C (black left–triangles) using a 4.5 at.% Ni isoconcentration surface. The $\pm 2\sigma$ error bars are based on counting statistics. For the major elements, the error bars are smaller than the marker size.

Figure 7. (a) An SEM image of an APT specimen tip illustrating $M_{23}C_6$ carbides interspersed along the *δ*–ferrite/*γ*–austenite heterophase interface in CF–8. (b) APT reconstruction of the same unaged CF–8 data set as in Fig. 5(a), with a 2.5 at.% C isoconcentration surface to better visualize the $M_{23}C_6$ carbide phase. Reconstruction dimensions: 94 nm × 61 nm. 0% of the Fe (blue) ions, 30% of the Cr ions (magenta), and 100% of Ni (green), Mn (mustard), Si (gray), Mo (red), and C (black) are depicted for clarity. (c) Rotated view of Fig. 6(b) to show that the carbide intersects the edge of the reconstruction volume. (d) One-dimensional (1D) concentration profiles using a 1 nm × 1 nm × 30 nm rectangular region of interest (ROI) seen in Fig. 6(b) for Fe (blue circles), Ni (green squares), Mn (mustard stars), Cr (magenta triangles), Si (gray diamonds), Mo (red asterisks), and C (black left–triangles) across the carbide phase. The $\pm$ 2σ error bars are based on counting statistics.

Figure 8. Conventional TEM images of the *δ*–ferrite/*γ*–austenite heterophase interface in (a) CF–3 and (b) CF–8 duplex stainless steels with (insets) selected area electron diffraction (SAED) patterns along a f.c.c. *γ*–austenite [001] zone axis.

Figure 9. (a) – (b) Conventional TEM images of an $M_{23}C_6$ carbide observed at the heterophase interface in CF–8 duplex stainless steel with (c) associated SAED pattern of the f.c.c. carbide along the *γ*–austenite/$M_{23}C_6$ $[\bar{3}01]$ zone axis and (d) TEM-EDS scan results of element concentrations taken along a 430 nm line across the $M_{23}C_6$ carbide from the *δ*–ferrite phase to the *γ*–austenite phase along the dashed arrow in Fig. 9(b).

Figure 10. (a) An example region of interest (ROI) illustrating the compositional heterogeneity of alternating Fe-rich *α*–domains (blue), Cr-rich *α'*–domains (magenta), and a Ni-rich G–phase precipitate (green) with (b) corresponding Fe, Cr, and Ni concentration profiles for CF–8 specimen aged to 4300 h at 400 ^{o}C. The Fe and Cr mean concentrations are superimposed in the plot as solid horizontal lines.

Figure 11. Distribution histograms of Cr with superimposed random binomial distribution curves for unaged (a) CF–3 wavelength, (b) CF–8 wavelength, (c) CF–3 amplitude, and (d) CF–8 amplitude.

Figure 12. (a) The mean wavelength (MW) and (b) mean amplitude (MA) values of CF–3 (solid symbols) and CF–8 (open symbols) are plotted as a function of aging temperatures: unaged (diamonds) and specimens aged to 4300 h at 280 °C (circles), 320 °C (squares), 360 °C (triangles), and 400 °C (stars). The MW values (black) are compared to the auto correlation function (ACF) method wavelengths (blue) and the MA values (black) are compared to the Langer Bar-on Miller (LBM) method amplitudes (red). The ACF and LBM method values are staggered to the right of the MW and MA values by 5 ^{o}C for clarity. The mean wavelength (MW) of (c) CF–3 and (e) CF–8 and the mean amplitude (MA) of (d) CF–3 and (f) CF–8 are plotted as a function of aging time. Solid symbols indicate CF–3 while open symbols indicate CF–8. Trend lines from the unaged data to the aged data are drawn with corresponding colors. The operational temperatures (280 °C and 320 °C) are solid lines, while the accelerated temperatures (360 °C and 400 °C) are dashed lines.

Figure 13. (a) Series of APT reconstructions illustrating G–phase precipitates in the decomposing *δ*–ferrite phase delineated by 6.5 at.% Ni (green) isoconcentration surfaces in unaged and 4300 h aged CF–3 specimens. (b) Series of G–phase precipitates delineated by 6.5 at.% Ni (green) isoconcentration surfaces in unaged and 4300 h aged CF–8 specimens. The G–phase precipitates are only observed in CF–3 aged at 360 °C and 400 °C, and CF–8 aged at 400 °C. The *γ*–austenite phase has a Ni concentration greater than the 6.5 at.% threshold and thus is displayed as large green isosurfaces. Only displaying 10% of the Ni (green) atoms for clarity.

Figure 14. Example G–phase precipitate proximity histogram concentration profiles in CF–8 aged to 4300 h at 400 ^{o}C for Fe (blue circles), Ni (green squares), Mn (mustard stars), Cr (magenta triangles), Si (gray diamonds), Mo (red asterisks), and Cu (orange right–triangles) using a 6.5 at.% Ni isoconcentration surface. The $\pm$ 2σ error bars are based on counting statistics. For the major elements, the error bars are smaller than the marker size.

List of Figures

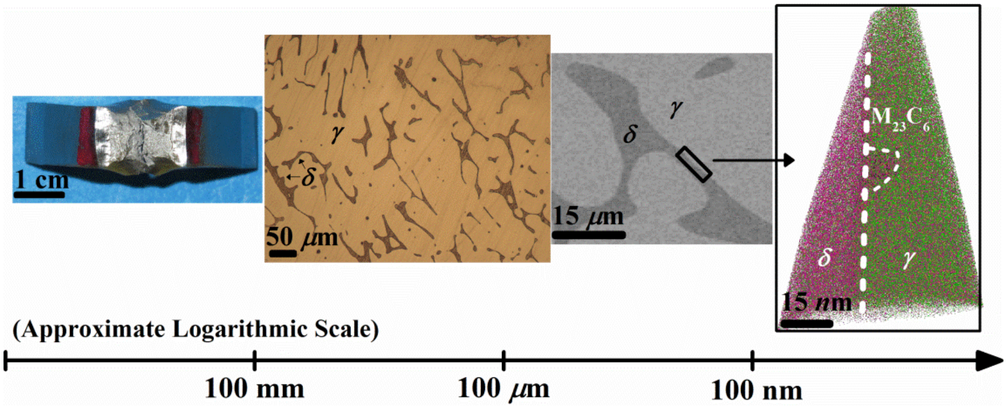

Graphical Abstract

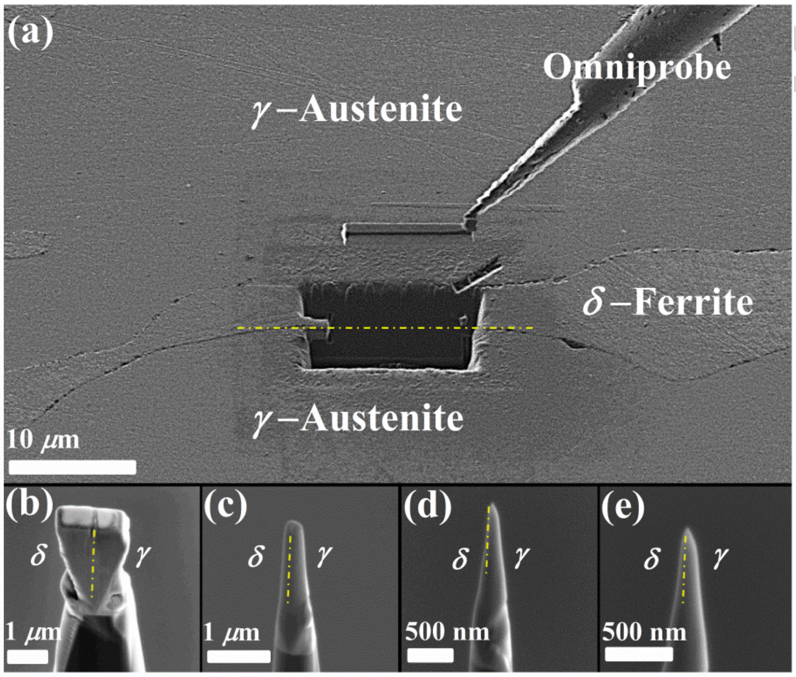

Figure 1

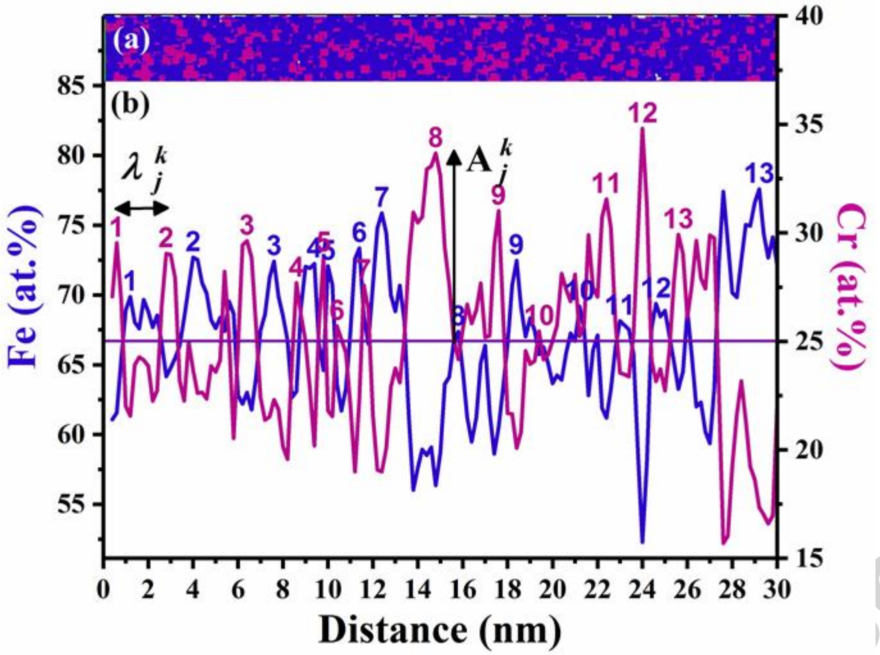
(a)
(b)
Fe (at.%)
Cr (at.%)
Distance (nm)
λ
k
j
A
k
j
85
80
75
70
65
60
55
40
35
30
25
20
15
0
2
4
6
8
10
12
14
16
18
20
22
24
26
28
30
1
2
3
4
5
6
7
8
9
10
11
12
13

Figure 2

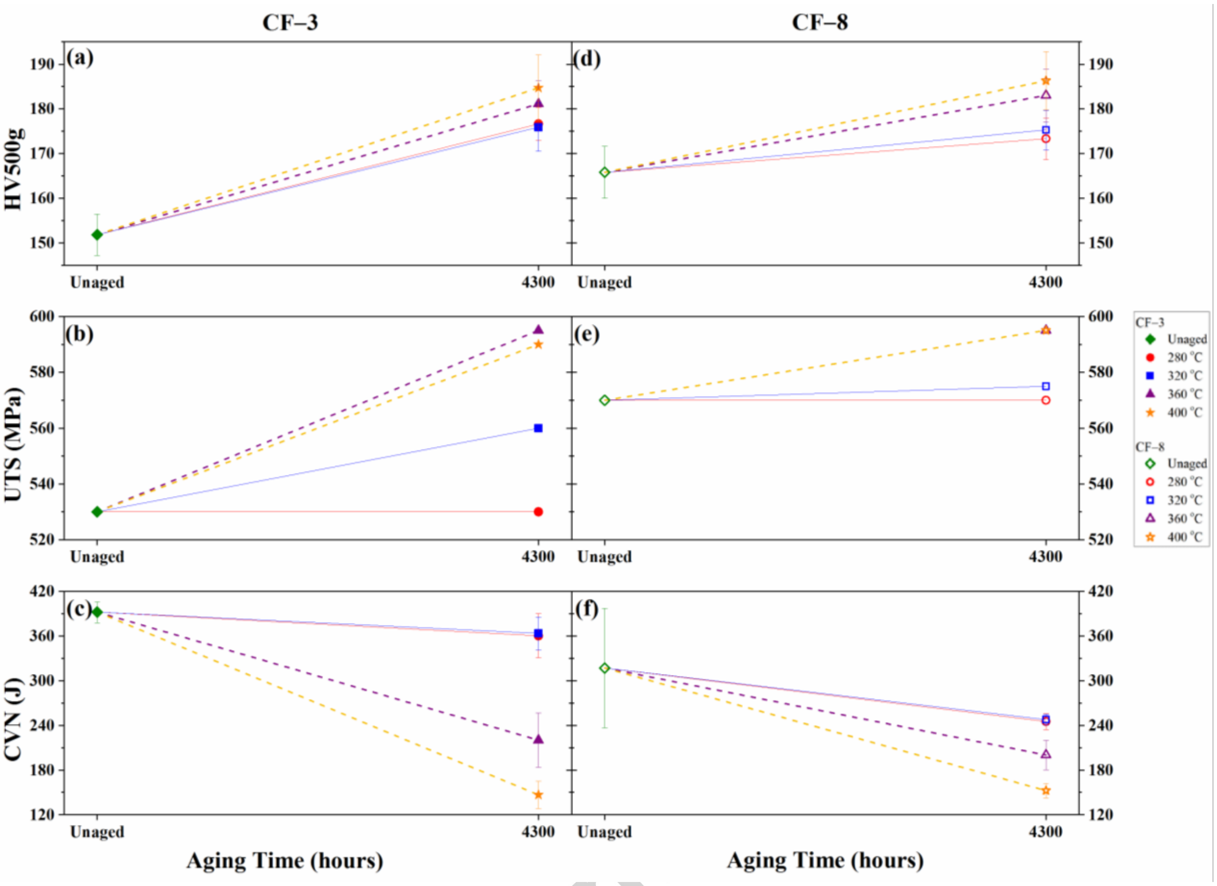
CF−3
CF−8
(a)
(b)
(c)
(d)
(e)
(f)
HV500g
UTS (MPa)
CVN (J)
190
180
170
160
150
600
580
560
540
520
420
360
300
240
180
120
Unaged
4300
Aging Time (hours)
CF−3
◆ Unaged
● 280 °C
■ 320 °C
▲ 360 °C
★ 400 °C
CF−8
◇ Unaged
○ 280 °C
□ 320 °C
△ 360 °C
☆ 400 °C

Figure 3

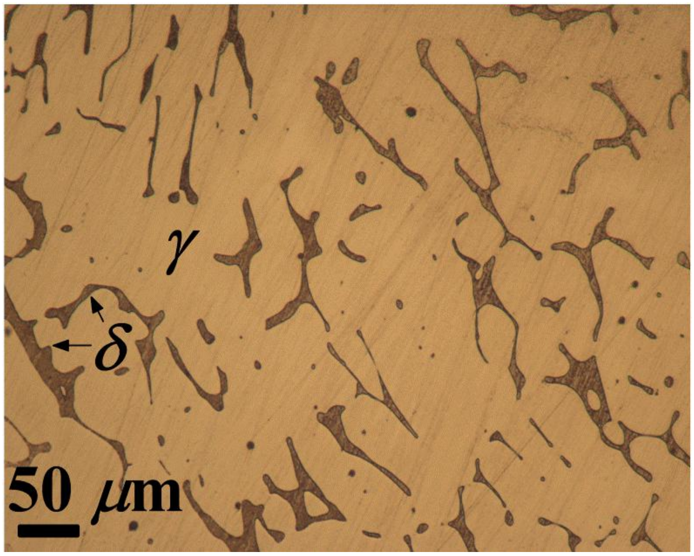

Figure 4

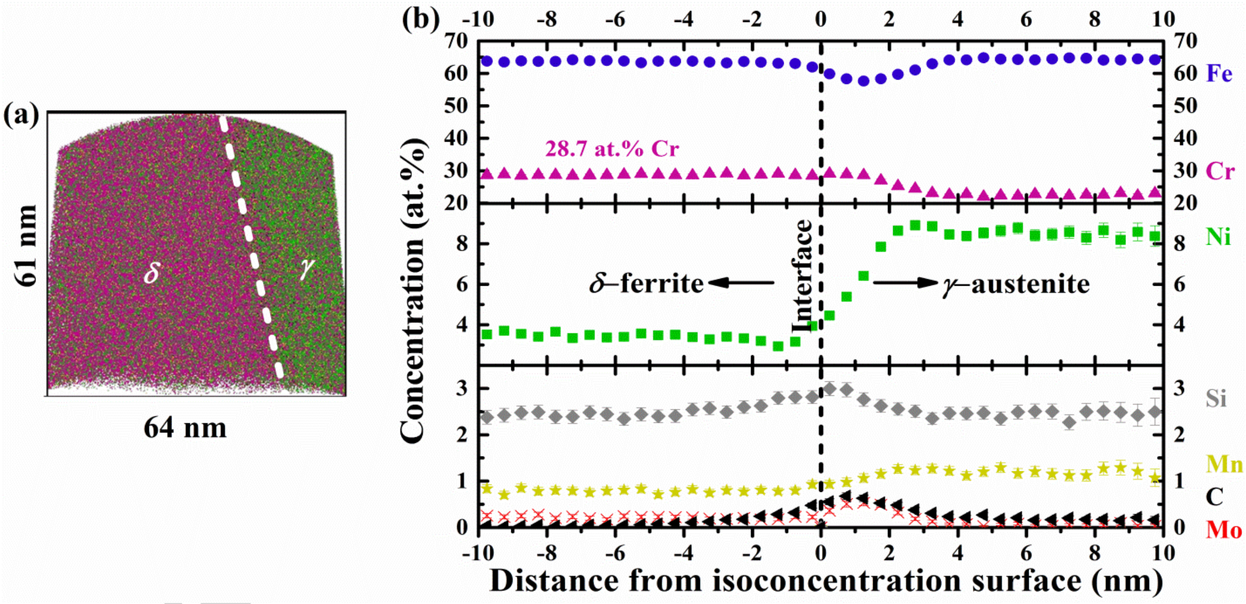

Figure 5

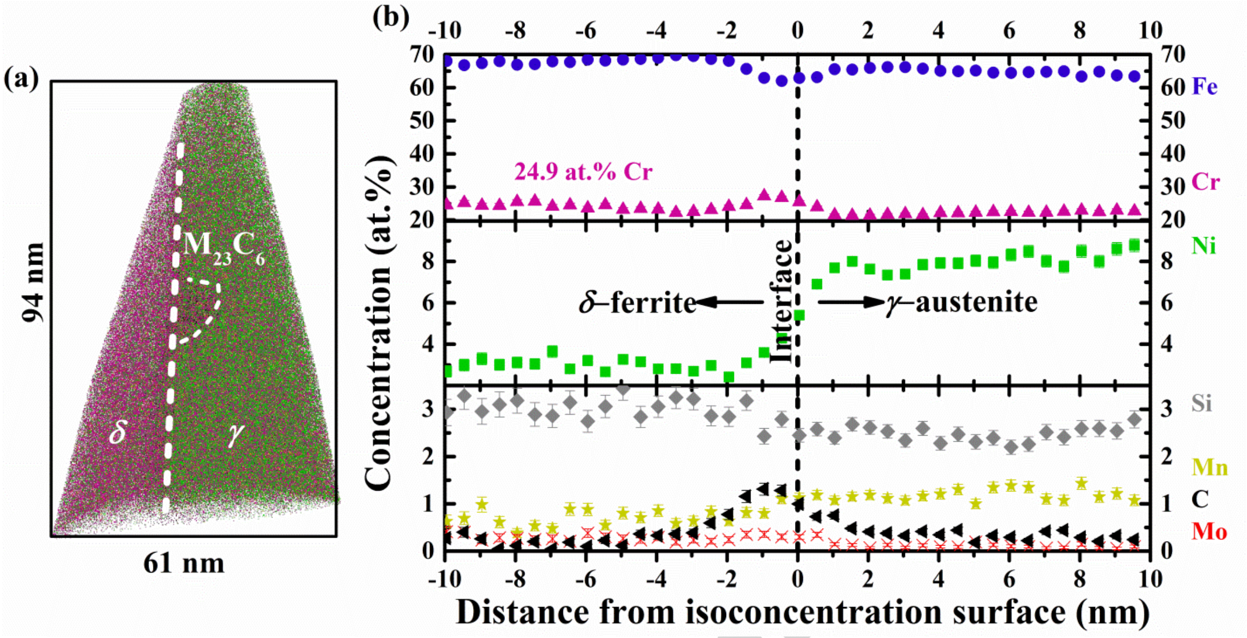

Figure 6

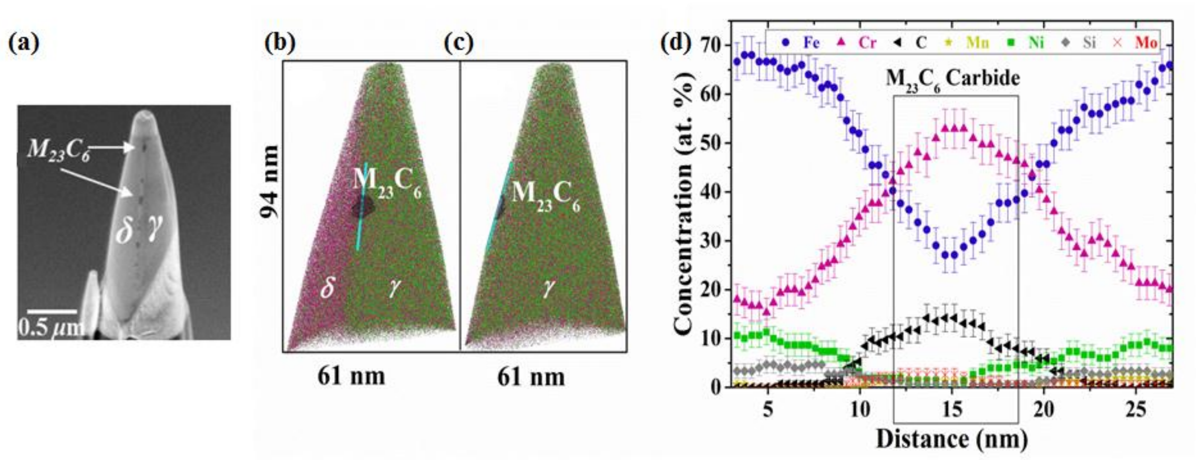

Figure 7

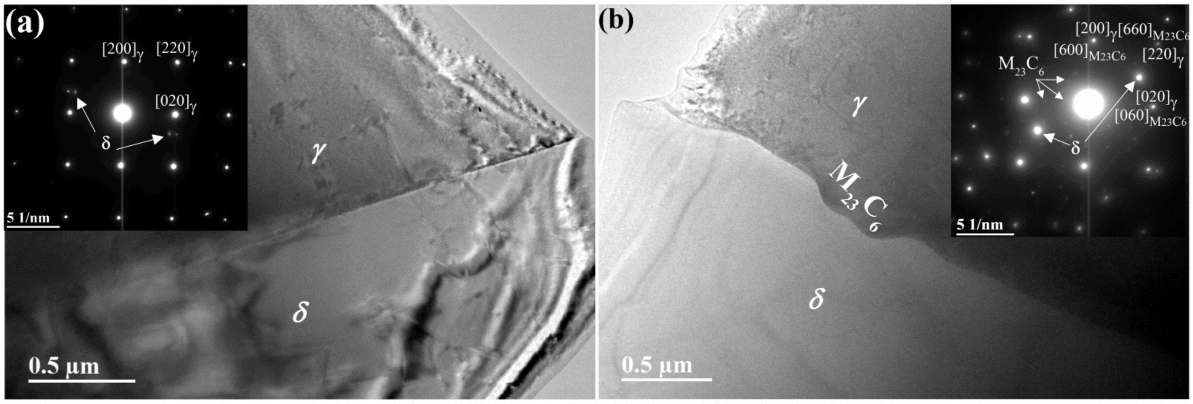

Figure 8

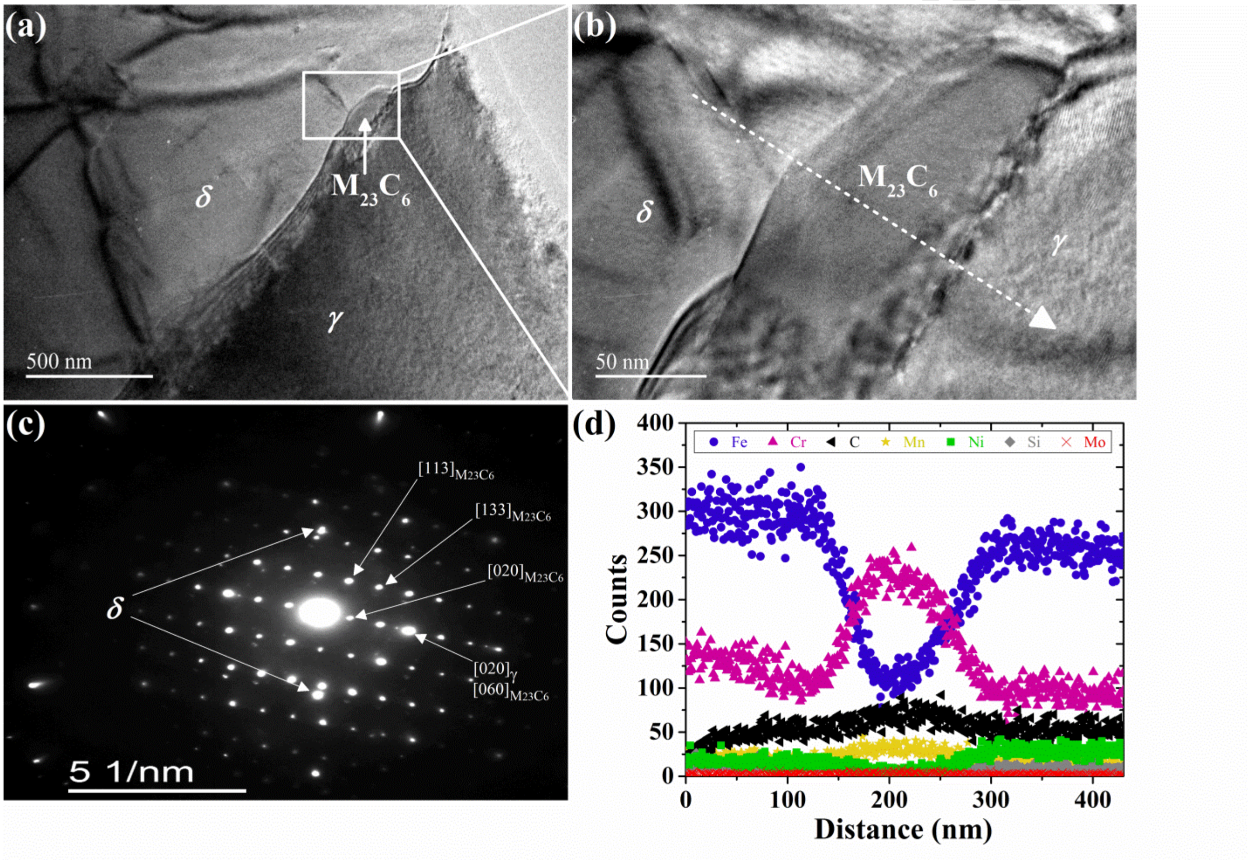

Figure 9

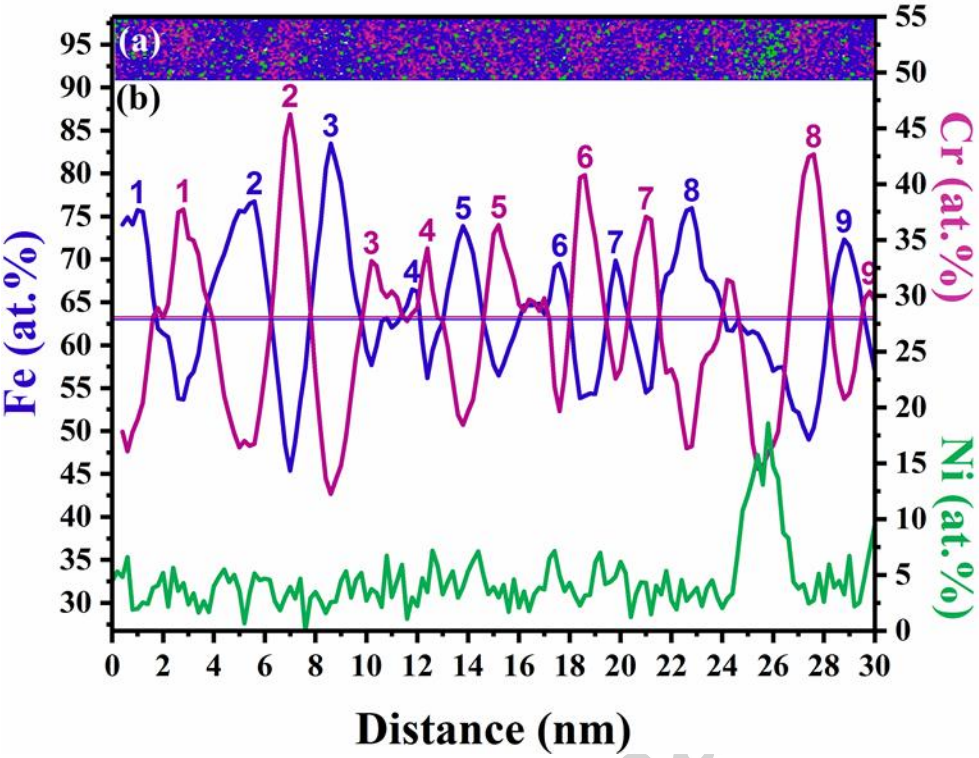
(a)
(b)
Fe (at.%)
Cr (at.%)
Ni (at.%)
Distance (nm)
95
90
85
80
75
70
65
60
55
50
45
40
35
30
55
50
45
40
35
30
25
20
15
10
5
0
0 2 4 6 8 10 12 14 16 18 20 22 24 26 28 30
1 2 3 4 5 6 7 8 9
1 2 3 4 5 6 7 8 9

Figure 10

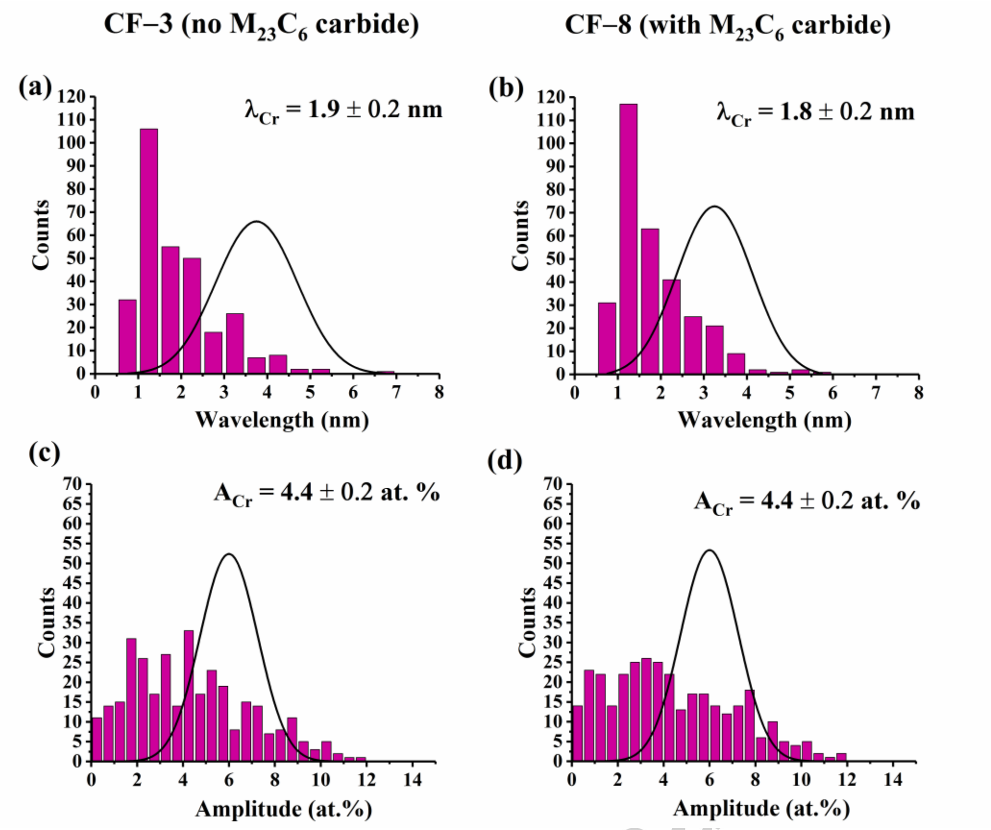
CF−3 (no $M_{23}C_6$ carbide)
CF−8 (with $M_{23}C_6$ carbide)
(a)
λ_{Cr} = 1.9 ± 0.2 nm
Counts
Wavelength (nm)
(b)
λ_{Cr} = 1.8 ± 0.2 nm
Counts
Wavelength (nm)
(c)
A_{Cr} = 4.4 ± 0.2 at. %
Counts
Amplitude (at.%)
(d)
A_{Cr} = 4.4 ± 0.2 at. %
Counts
Amplitude (at.%)

Figure 11

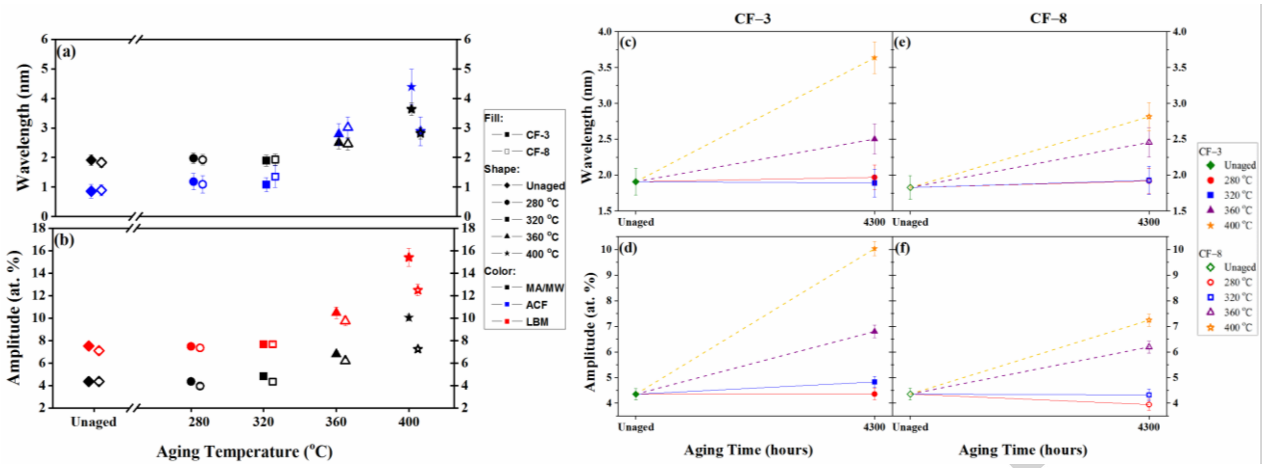
(a)
Wavelength (nm)
(b)
Amplitude (at. %)
Unaged
280
320
360
400
Aging Temperature (°C)
Fill:
CF-3
CF-8
Shape:
Unaged
280 °C
320 °C
360 °C
400 °C
Color:
MA/MW
ACF
LBM
CF–3
CF–8
(c)
(e)
(d)
(f)
Wavelength (nm)
Amplitude (at. %)
Unaged
4300
Aging Time (hours)
CF-3
Unaged
280 °C
320 °C
360 °C
400 °C
CF-8
Unaged
280 °C
320 °C
360 °C
400 °C

Figure 12

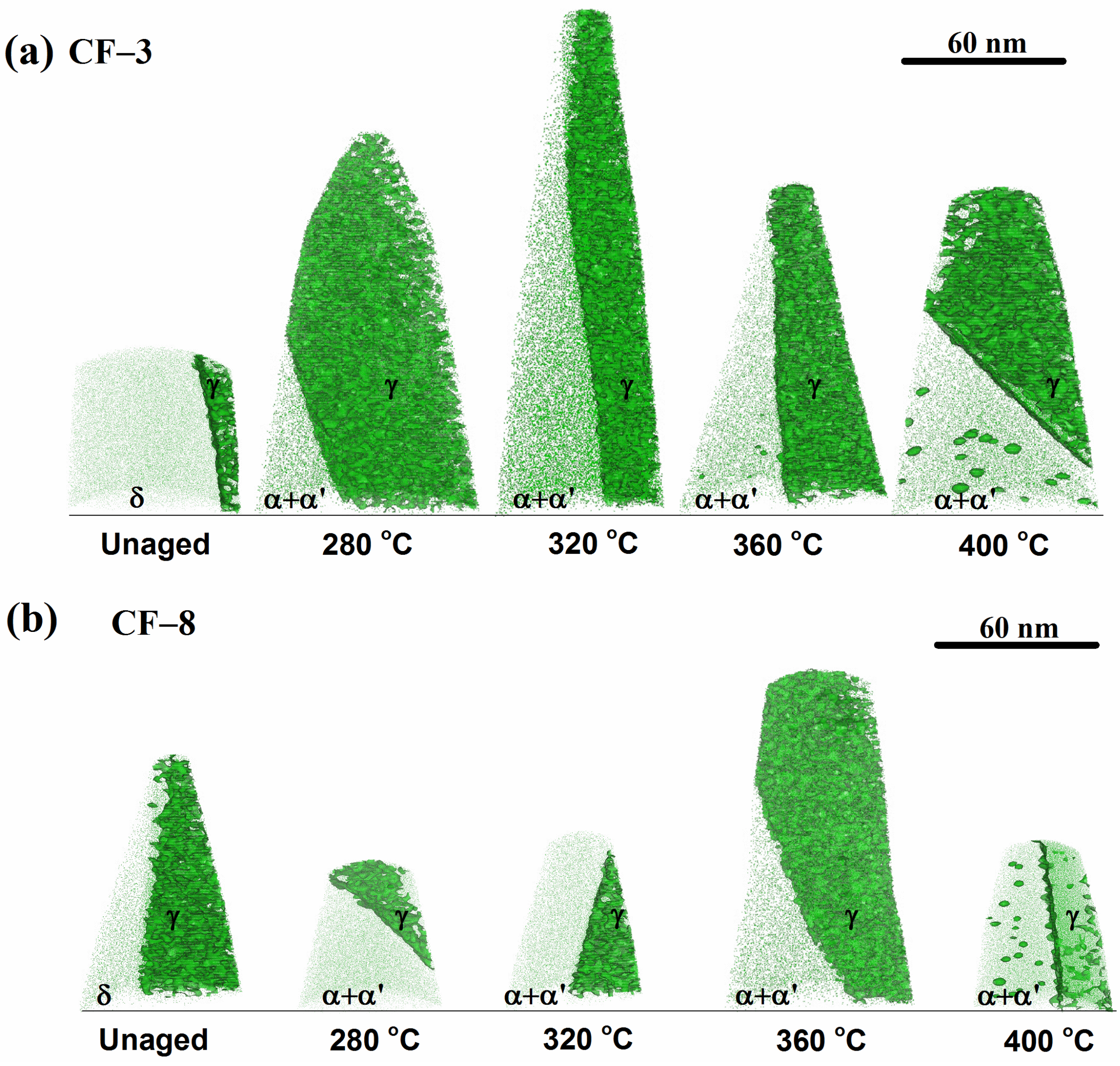
(a) CF–3
60 nm
γ
δ
α+α'
Unaged
280 °C
320 °C
360 °C
400 °C
(b) CF–8
60 nm
γ
δ
α+α'
Unaged
280 °C
320 °C
360 °C
400 °C

Figure 13

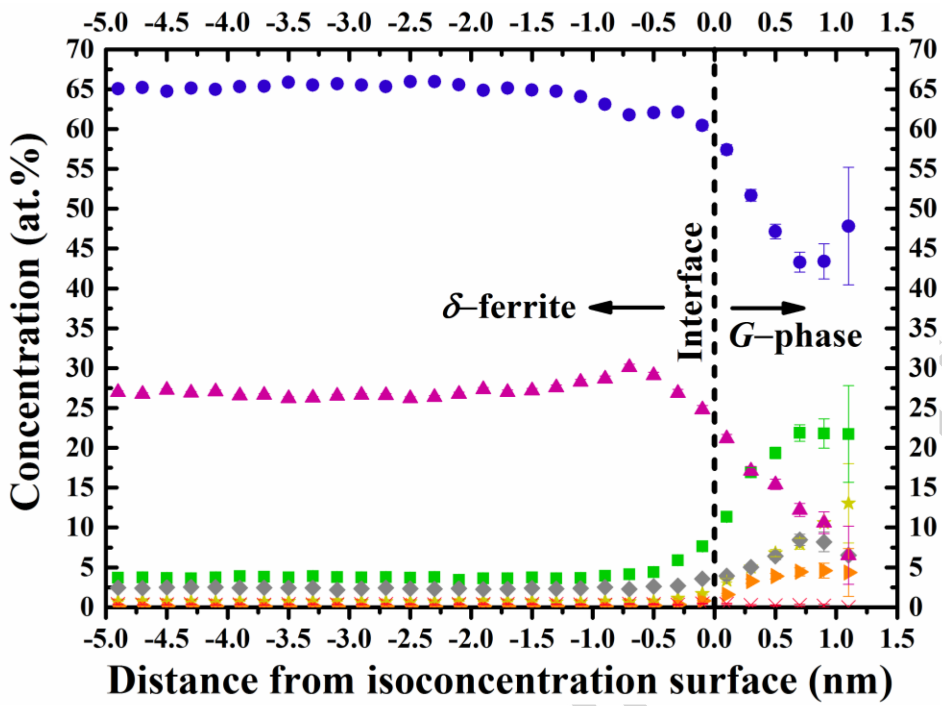

Figure 14

References

[1] J. K. Sahu, U. Krupp, R. N. Ghosh, and H.-J. Christ, “Effect of 475 °C embrittlement on the mechanical properties of duplex stainless steel,” *Materials Science and Engineering: A*, vol. 508, no. 1–2, pp. 1–14, May 2009.

[2] Y. Chen, B. Alexandreanu, K. Natesan, and A. S. Rao, “Environmentally assisted cracking and irradiation embrittlement of CF-8 and CF-8M cast austenitic stainless steels in high-purity water,” *Nuclear Energy Agency of the OECD (NEA)*, 2015.

[3] R. P. Kolli *et al.*, “Characterization of Element Partitioning at the Austenite/Ferrite Interface of asCast CF-3 and CF-8 Duplex Stainless Steels,” *Microscopy and Microanalysis*, no. Supplement S3, pp. 365–366, Aug. 2015.

[4] Z.-X. Wang, F. Xue, W.-H. Guo, H.-J. Shi, G.-D. Zhang, and G. Shu, “Investigation of thermal aging damage mechanism of the Cast Duplex Stainless Steel,” *Nuclear Engineering and Design*, vol. 240, no. 10, pp. 2538–2543, Oct. 2010.

[5] M. K. Miller and J. Bentley, “APFIM and AEM investigation of CF8 and CF8M primary coolant pipe steels,” *Materials Science and Technology*, vol. 6, no. 3, pp. 285–292, Mar. 1990.

[6] F. Danoix and P. Auger, “Atom Probe Studies of the Fe–Cr System and Stainless Steels Aged at Intermediate Temperature: A Review,” *Materials Characterization*, vol. 44, no. 1–2, pp. 177–201, Jan. 2000.

[7] P. Auger, F. Danoix, A. Menand, S. Bonnet, J. Bourgoin, and M. Guttmann, “Atom probe and transmission electron microscopy study of aging of cast duplex stainless steels,” *Materials Science and Technology*, vol. 6, no. 3, pp. 301–313, Mar. 1990.

[8] P. McConnell, W. Sheckherd, and D. Norris, “Properties of thermally embrittled cast duplex stainless steel,” *Journal of Materials Engineering*, vol. 11, no. 3, pp. 227–236, Dec. 1989.

[9] P. H. Pumphrey and K. N. Akhurst, “Aging kinetics of CF3 cast stainless steel in temperature range 300–400°C,” *Materials Science and Technology*, vol. 6, no. 3, pp. 211–220, Mar. 1990.

[10] H. M. Chung, “Aging and life prediction of cast duplex stainless steel components,” *International Journal of Pressure Vessels and Piping*, vol. 50, no. 1, pp. 179–213, Jan. 1992.

[11] H. M. Chung and T. R. Leax, “Embrittlement of laboratory and reactor aged CF3,CF8, and CF8M duplex stainless steels,” *Materials Science and Technology*, vol. 6, no. 3, pp. 249–262, Mar. 1990.

[12] C. Pareige, S. Novy, S. Saillet, and P. Pareige, “Study of phase transformation and mechanical properties evolution of duplex stainless steels after long term thermal ageing (>20 years),” *Journal of Nuclear Materials*, vol. 411, no. 1–3, pp. 90–96, Apr. 2011.

[13] O. K. Chopra, *Initial assessment of the mechanisms and significance of low-temperature embrittlement of cast stainless steels in LWR systems*. Division of Engineering, Office of Nuclear Regulatory Research, U.S. Nuclear Regulatory Commission, 1990.

[14] O. K. Chopra and G. Ayrault, “Aging degradation of cast stainless steel: Status and program,” *Nuclear Engineering and Design*, vol. 86, no. 1, pp. 69–77, Apr. 1985.

[15] O. K. Chopra and H. M. Chung, “Aging of cast duplex stainless steels in LWR systems,” *Nuclear Engineering and Design*, vol. 89, no. 2–3, pp. 305–318, Nov. 1985.

[16] T. S. Byun, Y. Yang, N. R. Overman, and J. T. Busby, “Thermal Aging Phenomena in Cast Duplex Stainless Steels,” *Journal of the Minerals, Metals, and Materials Society*, vol. 68, no. 2, pp. 507–516, Nov. 2015.

[17] S. Bonnet, J. Bourgoin, J. Champredonde, D. Guttmann, and M. Guttmann, “Relationship between evolution of mechanical properties of various cast duplex stainless steels and metallurgical and aging parameters: outline of current EDF programmes,” *Materials Science and Technology*, vol. 6, no. 3, pp. 221–229, Mar. 1990.

[18] S. Mburu *et al.*, “Atom Probe Tomography Analysis of the Local Chemical Environment at the Austenite/Ferrite Interfaces of Cast Duplex Stainless Steels,” *“Engineering Innovation for Global Sustainability”: Proceedings of the 14th LACCEI International Multi-Conference for Engineering, Education, and Technology*, Jul. 2016.

[19] O. K. Chopra and H. M. Chung, “Effect of Low-Temperature Aging on the Mechanical Properties of Cast Stainless Steels,” Argonne National Lab., IL (USA), CONF-871232-2, Jul. 1987.

[20] T. Hamaoka, A. Nomoto, K. Nishida, K. Dohi, and N. Soneda, “Accurate determination of the number density of G-phase precipitates in thermally aged duplex stainless steel,” *Philosophical Magazine*, vol. 92, no. 22, pp. 2716–2732, Aug. 2012.

[21] T. Hamaoka, A. Nomoto, K. Nishida, K. Dohi, and N. Soneda, “Effects of aging temperature on G-phase precipitation and ferrite-phase decomposition in duplex stainless steel,” *Philosophical Magazine*, vol. 92, no. 34, pp. 4354–4375, Dec. 2012.

[22] J. Emo, C. Pareige, S. Saillet, C. Domain, and P. Pareige, “Kinetics of secondary phase precipitation during spinodal decomposition in duplex stainless steels: A kinetic Monte Carlo model – Comparison with atom probe tomography experiments,” *Journal of Nuclear Materials*, vol. 451, no. 1–3, pp. 361–365, Aug. 2014.

[23] D. Isheim, R. P. Kolli, M. E. Fine, and D. N. Seidman, “An atom-probe tomographic study of the temporal evolution of the nanostructure of Fe–Cu based high-strength low-carbon steels,” *Scripta materialia*, vol. 55, no. 1, pp. 35–40, 2006.

[24] A. Devaraj *et al.*, “Three-dimensional nanoscale characterisation of materials by atom probe tomography,” *International Materials Reviews*, Jan. 2017.

[25] J. W. Cahn, “On spinodal decomposition,” *Acta Metallurgica*, vol. 9, no. 9, pp. 795–801, Sep. 1961.

[26] J. W. Cahn and J. E. Hilliard, “Free Energy of a Nonuniform System. I. Interfacial Free Energy,” *The Journal of Chemical Physics*, vol. 28, no. 2, pp. 258–267, Feb. 1958.

[27] M. K. Miller, J. M. Hyde, M. G. Hetherington, A. Cerezo, G. D. W. Smith, and C. M. Elliott, “Spinodal decomposition in Fe-Cr alloys: Experimental study at the atomic level and comparison with computer models—I. Introduction and methodology,” *Acta Metallurgica et Materialia*, vol. 43, no. 9, pp. 3385–3401, Sep. 1995.

[28] M. K. Miller, A. Cerezo, M. G. Hetherington, and J. M. Hyde, “Estimation of composition amplitude: Pa and LBM versus V,” *Surface Science*, vol. 266, no. 1, pp. 446–452, Apr. 1992.

[29] M. K. Miller, K. F. Russell, K. Thompson, R. Alvis, and D. J. Larson, “Review of Atom Probe FIB-Based Specimen Preparation Methods,” *Microscopy and Microanalysis*, vol. 13, no. 06, pp. 428–436, Dec. 2007.

[30] K. Thompson, D. Lawrence, D. J. Larson, J. D. Olson, T. F. Kelly, and B. Gorman, “In situ site-specific specimen preparation for atom probe tomography,” *Ultramicroscopy*, vol. 107, no. 2–3, pp. 131–139, Feb. 2007.

[31] R. P. Kolli and F. Meisenkothen, “A Focused Ion Beam Specimen Preparation Method to Minimize Gallium Ion Concentration in Copper Atom-Probe Tomography Specimen Tips,” *Microscopy and Microanalysis*, vol. 20, no. S3, pp. 350–351, 2014.

[32] O. C. Hellman, J. A. Vandenbroucke, J. Rüsing, D. Isheim, and D. N. Seidman, “Analysis of Three-dimensional Atom-probe Data by the Proximity Histogram,” *Microscopy and Microanalysis*, vol. 6, no. 05, pp. 437–444, Sep. 2000.

[33] R. P. Kolli and D. N. Seidman, “Comparison of compositional and morphological atom-probe tomography analyses for a multicomponent Fe-Cu steel,” *Microscopy and Microanalysis*, vol. 13, no. 4, pp. 272–284, Aug. 2007.

[34] B. Gault, M. P. Moody, J. M. Cairney, and S. P. Ringer, *Atom Probe Microscopy*, vol. 160. New York, NY: Springer New York, 2012.

[35] M. D. Mathew, L. M. Lietzan, K. L. Murty, and V. N. Shah, “Low temperature aging embrittlement of CF-8 stainless steel,” *Materials Science and Engineering: A*, vol. 269, no. 1–2, pp. 186–196, Aug. 1999.

[36] W. F. Michaud, P. T. Toben, W. K. Soppet, and O. K. Chopra, *Tensile-property characterization of thermally aged cast stainless steels*. Washington, DC: Division of Engineering, Office of Nuclear Regulatory Research, U.S. Nuclear Regulatory Commission, 1994.

[37] S. C. Schwarm, R. P. Kolli, E. Aydogan, S. Mburu, and S. Ankem, "Characterization of phase properties and deformation in ferritic-austenitic duplex stainless steels by nanoindentation and finite element method," *Materials Science and Engineering: A*, vol. 680, pp. 359–367, 2017.

[38] S. C. Schwarm, S. Mburu, R. P. Kolli, D. E. Perea, J. Liu, and S. Ankem, "Mechanical and Microstructural Effects of Thermal Aging on Cast Duplex Stainless Steels by Experiment and Finite Element Method," in *Mechanical and Creep Behavior of Advanced Materials*, I. Charit, Y. T. Zhu, S. A. Maloy, and P. K. Liaw, Eds. Springer International Publishing, 2017, pp. 253–262.

[39] S. L. Li *et al.*, "Microstructure evolution and impact fracture behaviors of Z3CN20-09M stainless steels after long-term thermal aging," *Journal of Nuclear Materials*, vol. 433, no. 1–3, pp. 41–49, Feb. 2013.

[40] Y. H. Yao, J. F. Wei, and Z. P. Wang, "Effect of long-term thermal aging on the mechanical properties of casting duplex stainless steels," *Materials Science and Engineering: A*, vol. 551, pp. 116–121, Aug. 2012.

[41] P. D. Southwick and R. W. K. Honeycombe, "Precipitation of M23C6 at austenite/ferrite interfaces in duplex stainless steel," *Metal Science*, vol. 16, no. 10, pp. 475–482, Oct. 1982.

[42] J. Y. Xie, N. X. Chen, L. D. Teng, and S. Seetharaman, "Atomistic study on the site preference and thermodynamic properties for Cr23−xFexC6," *Acta Materialia*, vol. 53, no. 20, pp. 5305–5312, Dec. 2005.

[43] J. J. Han, C. P. Wang, X. J. Liu, Y. Wang, and Z.-K. Liu, "First-principles calculation of structural, mechanical, magnetic and thermodynamic properties for γ-M 23 C 6 (M = Fe, Cr) compounds," *Journal of Physics: Condensed Matter*, vol. 24, no. 50, p. 505503, 2012.

[44] J. Janovec, A. Vyrostkova, and M. Svoboda, "Influence of tempering temperature on stability of carbide phases in 2.6cr-0.7mo-0.3v steel with various carbon content," *Metallurgical and Materials Transactions A*, vol. 25, no. 2, pp. 267–275, Feb. 1994.

[45] T. S. Byun, Y. Yang, N. R. Overman, and J. T. Busby, "Thermal Aging Phenomena in Cast Duplex Stainless Steels," *Journal of the Minerals, Metals, and Materials Society*, vol. 68, no. 2, pp. 507–516, Feb. 2016.

[46] *Phase Transformations in Metals and Alloys, Third Edition*, 3 edition. Boca Raton, FL: CRC Press, 2009.

[47] R. W. Balluffi, S. Allen, and W. C. Carter, *Kinetics of Materials*. John Wiley & Sons, 2005.

[48] R. P. Kolli and D. N. Seidman, "Co-Precipitated and Collocated Carbides and Cu-Rich Precipitates in a Fe–Cu Steel Characterized by Atom-Probe Tomography," *Microscopy and Microanalysis*, vol. 20, no. 06, pp. 1727–1739, Dec. 2014.

[49] P. I. Williams and R. G. Faulkner, "Chemical volume diffusion coefficients for stainless steel corrosion studies," *Journal of Materials Science*, vol. 22, no. 10, pp. 3537–3542, Oct. 1987.

[50] R. W. K. Honeycombe and R. F. Mehl, "Transformation from austenite in alloy steels," *Metallurgical Transactions A*, vol. 7, no. 7, pp. 915–936, Jul. 1976.

[51] H. K. D. H. Bhadeshia, "Diffusional formation of ferrite in iron and its alloys," *Progress in Materials Science*, vol. 29, no. 4, pp. 321–386, Jan. 1985.

[52] J. Zhou, J. Odqvist, M. Thuvander, and P. Hedström, “Quantitative evaluation of spinodal decomposition in Fe-Cr by atom probe tomography and radial distribution function analysis,” *Microscopy and Microanalysis*, vol. 19, no. 3, pp. 665–675, Jun. 2013.

[53] T. Kuwajima, Y. Saito, and Y. Suwa, “Kinetics of phase separation in iron-based ternary alloys. II. Numerical simulation of phase separation in Fe–Cr–X(X=Mo, Cu) ternary alloys,” *Intermetallics*, vol. 11, no. 11–12, pp. 1279–1285, 2003.

[54] Y. S. Yoshihiro Suwa, “Kinetics of Phase Separation in Fe-Cr-Mo Ternary Alloys,” *Materials Transactions A*, vol. 43, no. 2, pp. 271–276, 2002.

[55] K. H. Lo, C. H. Shek, and J. K. L. Lai, “Recent developments in stainless steels,” *Materials Science and Engineering: R: Reports*, vol. 65, no. 4–6, pp. 39–104, May 2009.

[56] Y. Matsukawa *et al.*, “The two-step nucleation of G-phase in ferrite,” *Acta Materialia*, vol. 116, pp. 104–113, Sep. 2016.

[57] F. Vurpillot, A. Bostel, and D. Blavette, “Trajectory overlaps and local magnification in three-dimensional atom probe,” *Applied Physics Letters*, vol. 76, no. 21, pp. 3127–3129, May 2000.

[58] T. R. Leax, S. S. Brenner, and J. A. Spitznagel, “Atom probe examination of thermally ages CF8M cast stainless steel,” *Metallurgical Transactions A*, vol. 23, no. 10, pp. 2725–2736, Oct. 1992.

[59] T. Yamada, S. Okano, and H. Kuwano, “Mechanical property and microstructural change by thermal aging of SCS14A cast duplex stainless steel,” *Journal of Nuclear Materials*, vol. 350, no. 1, pp. 47–55, Mar. 2006.

[60] W. Guo, D. A. Garfinkel, J. D. Tucker, D. Haley, G. A. Young, and J. D. Poplawsky, “An atom probe perspective on phase separation and precipitation in duplex stainless steels,” *Nanotechnology*, vol. 27, no. 25, p. 254004, 2016.